

Shear-velocity structure, radial anisotropy and dynamics of the Tibetan crust

Matthew R. Agius* and Sergei Lebedev

Geophysics Section, Dublin Institute for Advanced Studies, 5 Merrion Square, Dublin, Ireland. E-mail: matthew@cp.dias.ie

Accepted 2014 August 21. Received 2014 August 15; in original form 2014 April 5

SUMMARY

Geophysical and geological data suggest that Tibetan middle crust is a partially molten, mechanically weak layer, but it is debated whether this low-viscosity layer is present beneath the entire plateau, what its properties are, how it deforms, and what role it has played in the plateau's evolution. Broad-band seismic surface waves yield resolution in the entire depth range of the Tibetan crust and can be used to constrain its shear-wave velocity structure (indicative of crustal composition, temperature and partial melting) and radial anisotropy (indicative of the patterns of deformation). We measured Love- and Rayleigh-wave phase-velocity curves in broad period ranges (up to 7–200 s) for a few tens of pairs and groups of stations across Tibet, combining, in each case, hundreds of interstation measurements, made with cross-correlation and waveform-inversion methods. Shear-velocity profiles were then determined by extensive series of non-linear inversions of the data, designed to constrain the depth-dependent ranges of isotropic-average shear speeds and radial anisotropy. Shear wave speeds within the Tibetan middle crust are anomalously low and, also, show strong lateral variations across the plateau. The lowest mid-crustal shear speeds are found in the north and west of the plateau (~ 3.1 – 3.2 km s^{-1}), within a pronounced low-velocity zone. In southeastern Tibet, crustal shear wave speeds increase gradually towards southeast, whereas in the north, the change across the Kunlun Fault is relatively sharp. The lateral variations of shear speeds within the crust are indicative of those in temperature. A mid-crustal temperature of $800 \text{ }^\circ\text{C}$, reported previously, can account for the low shear velocities across Lhasa. In the north, the temperature is higher and exceeds the solidus, resulting in partial melting that we estimate at 3–6 per cent. Strong radial anisotropy is required by the data in western-central Tibet (>5 per cent) but not in northeastern Tibet. The amplitude of radial anisotropy in the crust does not correlate with isotropic-average shear speed (and, by inference, with crustal rock viscosity) or with surface elevation. Instead, radial anisotropy is related to the deformation pattern and is the strongest in regions experiencing extension (crustal flattening), as noted previously. The growth of Tibet by the addition of Indian crustal rocks into its crust from the south is reflected in the higher crustal seismic velocities (and, thus, lower temperatures) in the southern compared to northern parts of the plateau (more recently added rocks having had less time to undergo radioactive heating within the thickened Tibetan crust). Gravity-driven flattening—the basic cause of extension and normal faulting in the southern, western and central Tibet—is evidenced by pervasive radial anisotropy in the middle crust beneath the regions undergoing extension; the overall eastward flow of the crust is directed by the boundaries and motions of the lithospheric blocks that surround Tibet.

Key words: Surface waves and free oscillations; Seismic anisotropy; Crustal structure; Asia.

1 INTRODUCTION

Tibet is the world's largest and highest plateau, rising between the northward-moving India to the south and the relatively stable

Eurasia to the north (e.g. Molnar & Tapponnier 1975; Fielding *et al.* 1994; Hatzfeld & Molnar 2010). Regional-scale variations in the style of deformation across the plateau (from normal faulting in its central part to strike-slip and thrust faulting towards the periphery) indicate heterogeneity in deformation processes within it (e.g. Armijo *et al.* 1986; Yin & Harrison 2000; Taylor & Yin 2009; Elliott *et al.* 2010). The relatively smooth topography (Fig. 1), however, can be interpreted as evidence for relatively homogeneous rheology

* Now at: Dipartiment tal-Fizika, Fakultà tax-Xjenza, L-Università ta' Malta, Msida, Malta.

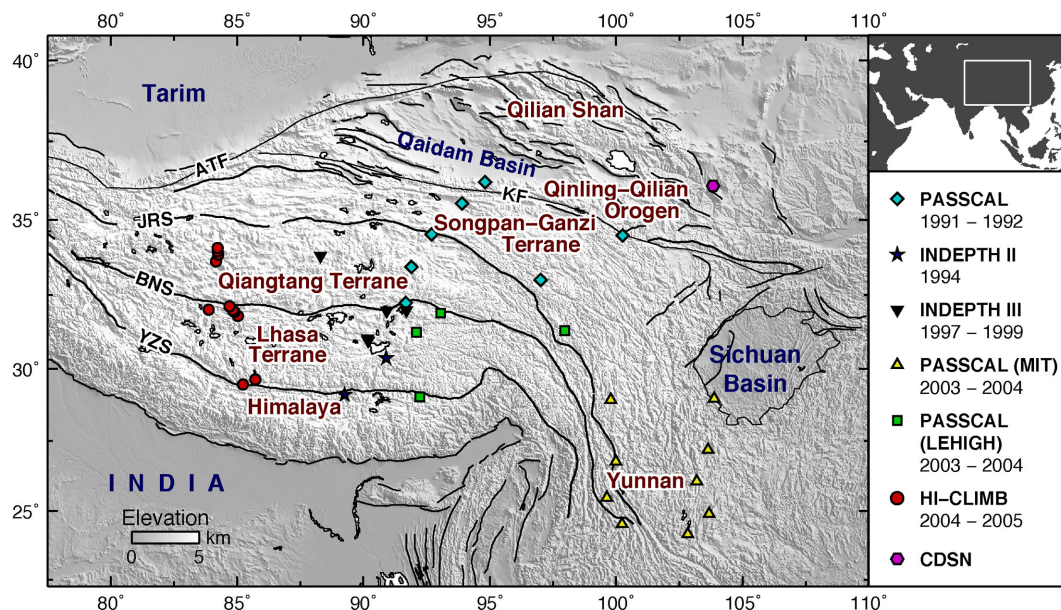


Figure 1. Seismic stations used in the surface wave measurements. Different symbols correspond to different networks deployed across the Tibetan Plateau. Black lines indicate sutures and faults: YZS (Yarlung-Zangbo Suture), BNS (Bangong-Nujiang Suture), JRS (Jinsha River Suture), KF (Kunlun Fault) and ATF (Altn Tagh Fault), which divide Tibet into major terranes. White shade highlights high elevation. Inset, top right: location of the map region within Asia.

of the deep crust (e.g. Bird 1991; Clark & Royden 2000; Royden *et al.* 2008).

Geophysical and geological observations suggest that the middle crust beneath at least parts of Tibet is partially molten and, thus, mechanically weak (e.g. Nelson *et al.* 1996; Wang *et al.* 2012b). Whether a low-viscosity layer is present beneath the entire plateau or only its portions is debated, as are the causes for and characteristics of this layer (e.g. Klempner 2006; Rippe & Unsworth 2010; Searle *et al.* 2011). Seismic-velocity models reveal strong lateral variations in the properties of the middle crust across the plateau (e.g. Yang *et al.* 2012), with radial anisotropy indicating different internal deformation patterns beneath its different parts (Shapiro *et al.* 2004). The relationships between the crustal structure and thickness, its temperature, composition, surface elevation and deformation must be understood in order for the dynamics of Tibetan crust to be determined. The continuous northward push of India and the on-going addition of new, India-derived material to the Tibetan crust play a key role in the dynamics and evolution of the plateau (e.g. Replumaz *et al.* 2010). Yet, how the addition of new crust is accommodated within Tibet is still debated (e.g. Kapp & Guynn 2004; Royden *et al.* 2008).

Seismic-wave velocities are commonly used to infer the temperature and composition of the rocks at depth (e.g. Christensen 1996; Kern *et al.* 2001; Mechie *et al.* 2004; Caldwell *et al.* 2009; Fulla *et al.* 2012; Yang *et al.* 2012). Estimates of the melt fraction and viscosity can also be derived (e.g. Watanabe 1993; Rosenberg & Handy 2005; Caldwell *et al.* 2009). An intracrustal low velocity zone (LVZ; defined here as a layer with shear velocity lower than that in the layers above and below) has been detected in Tibet using intermediate- and short-period surface wave data, inverted for 1-D crustal models (e.g. Chun & Yoshii 1977; Romanowicz 1982; Kind *et al.* 1996; Cotte *et al.* 1999; Rapine *et al.* 2003) and regional tomographic maps (e.g. Guo *et al.* 2009; Yang *et al.* 2012; Karplus *et al.* 2013; Li *et al.* 2013, 2014). The LVZ and the low resistivity zone at the same depth detected in magnetotelluric (MT) studies (e.g. Chen *et al.* 1996; Wei *et al.* 2001; Arora *et al.* 2007) have

been interpreted as evidence for the existence of the weak, partially molten layer within Tibetan mid-lower crust, prone to viscous flow (Nelson *et al.* 1996). Uncertainty remains, however, over how representative the various seismic and MT models are for the whole of Tibet, and to what extent they may be affected by anisotropy.

Tibet's crust is characterized by strong seismic anisotropy, both radial (Shapiro *et al.* 2004; Xie *et al.* 2013) and azimuthal (Huang *et al.* 2004; Su *et al.* 2008). Most published shear-speed models have been computed from Rayleigh-wave dispersion and, thus, represent vertically polarized shear waves only (V_{SV}). Hence, it is often uncertain whether the reported shear velocity decrease within the Tibetan mid-lower crust indicates a decrease in the isotropic-average seismic velocity—which depends on composition, temperature and the fraction of partial melt (if any) and which can be related to viscosity—or whether, instead, the low V_{SV} velocities are a result of strong radial anisotropy, reflecting alignment of anisotropic minerals by finite strain. Low S velocities due to high temperature and partial melting would decrease both V_{SV} and V_{SH} (horizontally polarized shear-wave speed), whereas radial anisotropy would result in divergence of the V_{SV} and V_{SH} values (e.g. Fulla *et al.* 2012).

Some of the published radially anisotropic S -velocity models, constrained by Love- and Rayleigh-wave data, do not display a LVZ for either V_{SV} or V_{SH} (Shapiro *et al.* 2004; Xie *et al.* 2013). 1-D models by Duret *et al.* (2010), averaging over long paths across much of Tibet, show only a small decrease in V_{SV} and an increase in V_{SH} from the upper-middle to the lower-middle crust. In contrast, the recent tomography of Yang *et al.* (2012), performed using ambient-noise, cross-correlation measurements for numerous interstation paths across Tibet, shows a very pronounced LVZ in V_{SV} , laterally continuous across large parts of the plateau, and with no obvious correlation to terrane boundaries within the high plateau. Tighter constraints on the shear-velocity and radial-anisotropy distributions within the Tibetan crust are needed to better our understanding of the structure and dynamics of the orogen.

In this study, we determine robust profiles of shear wave speed and radial anisotropy beneath different parts of Tibet. Using

non-linear inversions of new, broad-band (up to 7–200 s) Love and Rayleigh surface wave phase velocity measurements and considering ensembles of best-fitting models, we constrain shear-velocity structure from the upper crust down to the upper mantle. Assuming laboratory-based geophysical relationships, we then evaluate lateral variations of temperature and partial melt fraction within the crust. Finally, interpreting these results together with our new models of radial anisotropy and other available data on the structure and deformation of the plateau, we examine their implications for the dynamics of the Tibetan crust.

2 DATA AND MEASUREMENTS

The advantage of interstation measurements of surface wave phase velocities over source-station measurements typically used in large-scale tomography (Priestley *et al.* 2006; Lebedev & van der Hilst 2008; Schaeffer & Lebedev 2013) is that they can be made in broader period ranges (Meier *et al.* 2004; Lebedev *et al.* 2006; Agius & Lebedev 2013). Combining short and long period data is important in order to resolve trade-offs between model parameters from the upper crust down to the mantle. Furthermore, the use of local measurements brings the advantage of their simple, clear relationship to the local Earth structure. The small size of the inverse problem relating interstation dispersion curves to 1-D shear-velocity models enables us to constrain ranges of shear velocity and radial anisotropy beneath different parts of Tibet by means of targeted series of non-linear inversions.

2.1 Phase-velocity measurements

We measured broad-band, interstation, phase-velocity curves of Love and Rayleigh surface waves within west-central, central and eastern Tibet and surrounding regions. The pairs of stations were selected such that a large number of earthquake recordings suitable for the measurements were available. In total, 34 station pairs were selected. The broad-band stations belonged to various temporary networks [PASSCAL (91/92) (Owens *et al.* 1993), INDEPTH II and III (Nelson *et al.* 1996; Huang *et al.* 2000), HI-CLIMB (Nábělek *et al.* 2005), PASSCAL (Lehigh) (Sol *et al.* 2007), PASSCAL (MIT) (Lev *et al.* 2006)] and the permanent China Digital Seismic Network (Fig. 1). The seismograms were retrieved from the Incorporated Research Institutions for Seismology (IRIS) data centre. Automatic quality control on the data was performed to check for clipped and incomplete seismograms. The seismograms were then response-corrected to displacement, and the horizontal components were rotated to obtain the transverse component.

Surface wave dispersion measurements are made using a combination of two different, independent techniques: cross-correlation of seismograms from a pair of stations (Meier *et al.* 2004) and the derivation of interstation phase velocities from source-station measurements, performed using automated, multimode waveform fitting (Lebedev *et al.* 2005). In the first method, two vertical-component (for Rayleigh waves) or transverse-component (for Love waves) seismograms with recordings of the same earthquake at the two stations of a pair are cross-correlated. The cross-correlation function is filtered with a frequency-dependent bandpass filter. In order to enhance the signal-to-noise ratio and to down-weight side lobes resulting from correlations of the fundamental mode with scattered waves or higher modes, a frequency-dependent time window is applied. The fundamental-mode, phase velocity is then calculated from the phase of the cross-correlation function and the difference

of the distances between the source and each of the stations (Meier *et al.* 2004). The strength of this technique is that it can measure accurate phase velocities at both short (down to ~5 s) and long (>200 s) periods.

In the second method, we use the Automated Multimode Inversion (AMI) of surface and *S*-wave forms (Lebedev *et al.* 2005) to simultaneously fit *S*, multiple *S* and surface waves, using synthetic seismograms generated by mode summation. From the waveform fits of the seismograms recording the same earthquake at the two stations, we extract the fundamental-mode phase velocities and then calculate the interstation phase-velocity curves (Lebedev *et al.* 2006) as $(\Delta_2 - \Delta_1)/(\Delta_2/c_2 - \Delta_1/c_1)$, where Δ_1 , Δ_2 and c_1 , c_2 are the distances and average phase velocities between the source and each of the two stations. AMI's key strength, for the purposes of interstation dispersion analysis, is in its ability to determine phase velocities of long-period surface waves even when they interfere with energetic body waves. For the short and intermediate period surface waves with sensitivity primarily to the crust (periods below ~60 s, in the case of the thick Tibetan crust), we have obtained many more cross-correlation than waveform-inversion measurements (Fig. 2). The latter are still important, however, serving as a benchmark for the former and confirming that they are not biased by the interference of the fundamental and higher modes.

We restrict the selection of earthquakes to those approximately on the same great circle path with the two stations (station-earthquake backazimuths within less than 10° from the station-station azimuth). We select earthquakes listed in the Centroid Moment Tensor catalogue (e.g. Dziewonski *et al.* 1994), with moment magnitudes larger than about 4.8, and epicentral distances to the stations from 860 to 16 400 km. In an interactive selection, the smoothest portions of the fundamental-mode Rayleigh- and Love-wave dispersion curves are selected. Kinks or roughness in the curves are usually caused by diffraction of the fundamental mode or its interference with higher modes or with modes of the other type (Love for Rayleigh or Rayleigh for Love); rough portions of the curves are not accepted. Obvious outlier curves, away from the average, are also removed. We also looked for any systematic differences in phase-velocity measurements depending on the direction of the wave propagation between the two stations; these would be indicative of incorrect station timing or instrument response or a measurement bias due to diffraction, for waves coming from at least one of the directions. For the station pairs selected, no direction-dependent biases were detected. Averaging over a large number of one-event measurements, made using recordings of earthquakes in different source regions, in different directions from the station pair, results in robust measurements in broad period ranges.

Fig. 2 shows examples of Rayleigh- and Love-wave dispersion measurements. HI-CLIMB station pairs H0810–H1421 and H1050–H1350 are on nearly the same great-circle paths (Figs 2b and c) and thus have almost the same set of earthquakes used in the measurements (Figs 2f and g). Their close proximity also means that the surface waves sample nearly the same structure, resulting in very similar dispersion curves (Figs 2j–k and n–o). Note the numerous, superimposed, mutually consistent measurements from the different methods and opposite wave-propagation directions (Figs 2r and s). Many of the phase-velocity measurements include short periods (<10 s), sampling primarily the shallow, upper-crustal structure. Between 10 and 40 s periods, phase velocities are very low compared to global averages, due to the very thick crust beneath Tibet and low shear velocities within it. Between 40 and 60 s, phase velocities increase rapidly with period, approaching the reference values computed for the 1-D global reference model AK135

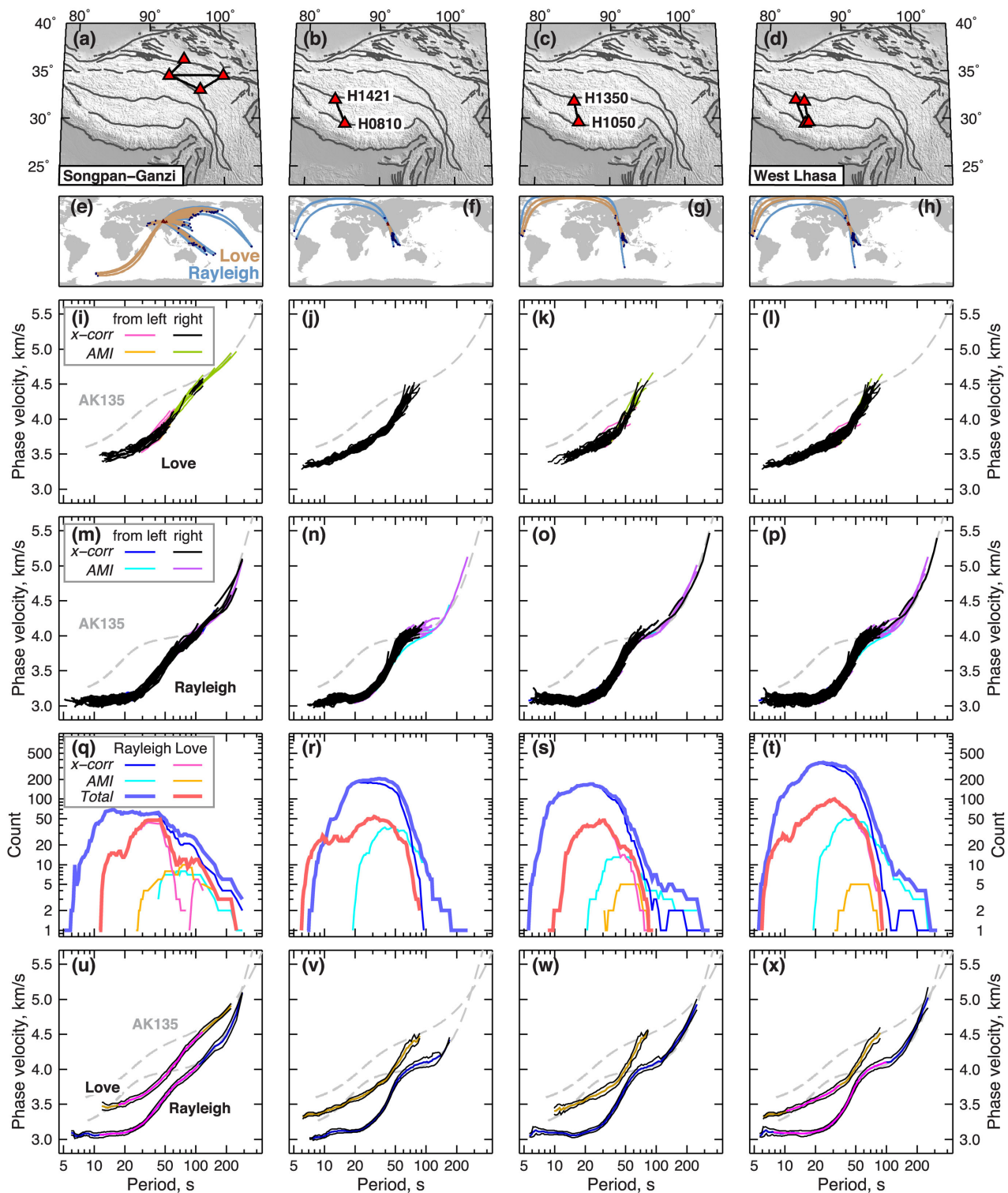


Figure 2. Phase-velocity measurements for station pairs and for region averages. The two columns in the middle illustrate interstation measurements for individual station pairs. The columns on the left-hand side and on the right-hand side show examples of region-average phase-velocity measurements, using all the data from all interstation pairs within the regions. Top row (a–d): the location of the station pairs (red triangles), and the interstation paths (black lines). Global maps (e–h): earthquakes (dark blue dots) and source-station great circle paths corresponding to Love-wave (brown) and Rayleigh-wave (cyan) measurements. The measured Love- and Rayleigh-wave dispersion curves are shown in (i–l) and (m–p), respectively. Different colours indicate the method and the direction each measurement corresponds to. AMI: measurements from the Automated Multimode Inversion technique (Lebedev *et al.* 2005). *x*-corr: measurements from the cross-correlation technique (Meier *et al.* 2004). Dashed grey curves show the phase velocities computed for the AK135 reference model (Kennett *et al.* 1995). Count graphs (q–t) show the total number of measurements at each period for Love and Rayleigh waves (red and blue, respectively); the lines in different colours show the counts from different methods. The bottom frame shows the resulting average dispersion curves for Love and Rayleigh waves and their standard deviations (black curves) (u–x); pink lines show the most robust portions of the curves selected to be used for the inversions.

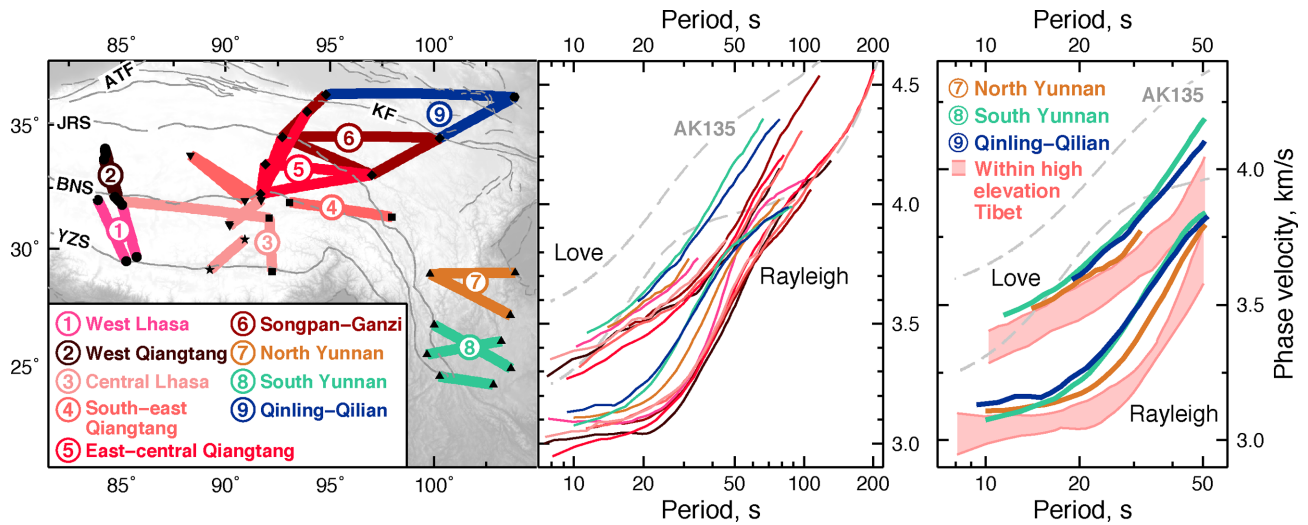


Figure 3. Phase-velocity curves measured in regions across the Tibetan Plateau. Left-hand panel: map showing inter-station paths within the nine colour-coded regions. Different symbols indicate stations of different networks, as in Fig. 1. Centre panel: the 9 Love-wave and 9 Rayleigh-wave, region-average, phase-velocity curves. Right-hand panel: comparison of region-average dispersion curves within the high-elevation part of the plateau (pink shade) and those from outside the high plateau. Dashed grey lines: dispersion curves computed for the AK135 reference model (Kennett *et al.* 1995).

(Kennett *et al.* 1995). For each path, the average phase velocity and the standard deviation are calculated at each period (Figs 2v and w). Dispersion-curve differences between the two paths (Figs 2j–k and n–o) are mostly at periods <20 s, likely due to shallow, upper crustal heterogeneity.

Although the average dispersion curves derived from our measurements are very smooth, and mostly with small standard deviations, there may be undetected biases remaining in the measurements. The sensitivity areas of interstation measurements can generally extend beyond the station-station corridor (de Vos *et al.* 2013), and phase velocities can be azimuthally dependent. In this paper, we base our inferences and conclusions only on robust, persistent patterns that are present in the data measured along multiple interstation paths. Regarding azimuthal anisotropy in particular, its amplitude within Tibetan crust, according to a number of recent surface wave studies (Yao *et al.* 2010; Yang *et al.* 2010; Agius & Lebedev 2014), is a few percent, smaller than the very large variations in radial anisotropy that we observe between different regions within Tibet. Therefore, even though the amplitude of radial anisotropy we report may be affected by the neglected azimuthal anisotropy, the main patterns and inferences we present are not.

2.2 Region-average measurements

Nearby station pairs are often located entirely within the same tectonic units and exhibit similar phase-velocity curves (Figs 2b and c). Thus, station pairs with similar dispersion curves can be grouped together, with the measurements combined so as to characterize the entire region. Figs 2(l) and (p) show the combined Love- and Rayleigh-wave measurements from the two station pairs in West Lhasa (Figs 2b and c). Combining dispersion curves together yields more robust, broad-band measurements, averaged from many hundreds of Love- and Rayleigh-wave curves. The region-average, phase-velocity curve and the corresponding standard deviation are calculated by averaging over all the measurements from all the pairs within the region at each period (Fig. 2x). Only the smoothest part of the curve is then selected, to be used in inversions (pink curve in the bottom frame).

In another example, Fig. 2(a) shows a group of differently aligned station pairs in the Songpan-Ganzi Terrane. Unlike in West Lhasa, the earthquakes used for the measurements at these pairs are distributed more widely across the globe since the interstation paths have different azimuths (Figs 2a and e). The dispersion curves from the individual station pairs are very similar, even though the pairs cover a region a few hundred kilometres across. The similarity of the dispersion curves indicates relatively homogeneous structure across this entire subregion.

We identify, empirically, nine subregions with weak phase-velocity variability within each: West Lhasa, Central Lhasa, West Qiangtang, East-central Qiangtang, Southeast Qiangtang, Songpan-Ganzi, North Yunnan, South Yunnan and Qinling-Qilian. Fig. 3 shows the interstation pairs within each region and also a comparison of the dispersion curves from different regions. All the nine regions show very low Love- and Rayleigh-wave phase velocities for periods less than 50 s, when compared to phase velocities computed for the global reference model AK135 (Kennett *et al.* 1995). Regions at highest elevations within Tibet display the lowest phase velocities (Fig. 3, regions 1–6). Between 10 and 20 s, Rayleigh- and Love-wave phase-velocity variations within the 9 regions are less than 0.2 km s^{-1} ; at the shortest periods they are likely to be due to sedimentary-layer and other upper-crustal heterogeneity.

Rayleigh-wave dispersion curve from West Qiangtang shows a dip (a minimum) at ~ 20 s. Between 30- and 40-s period, all six regions in the central, high-elevation part of the plateau are characterized by remarkably similar Rayleigh-wave phase velocities, suggesting a largely homogeneous structure within the deep crust. At periods longer than 40 s, phase velocities in West Lhasa increase rapidly with period, to exceed the global reference at 60-s period. This is due to presence of mantle lithosphere with very high seismic velocities beneath West Lhasa, interpreted previously to be the cold, cratonic lithosphere of India (Agius & Lebedev 2013). Phase velocities in other high-elevation parts of Tibet increase with period more gently, reflecting lower seismic velocities within the uppermost mantle beneath them.

The dispersion curves from Qinling-Qilian and South Yunnan, at the margins of the plateau where the crust is thinner than in Tibet proper, show relatively high phase velocities between

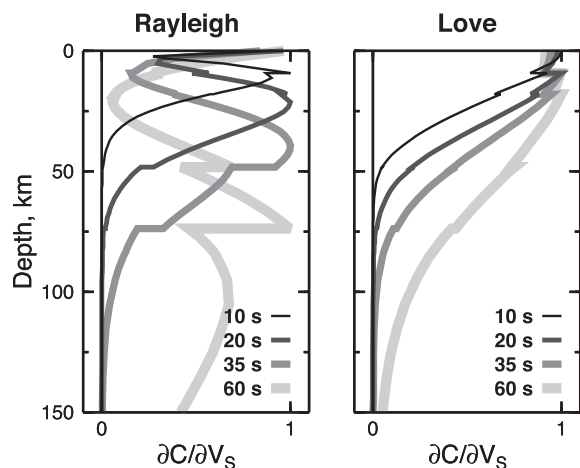


Figure 4. Depth sensitivity kernels for phase velocities of the fundamental-mode Rayleigh and Love waves. The curves for different periods are scaled independently. These kernels are computed for a 1-D shear velocity profile of West Lhasa, with a four-layer crust and a Moho discontinuity at 74 km depth.

20- and 50-s periods. The dispersion curves are very similar overall, indicating similar crustal structure and thickness at the northeastern and southeastern margins of the plateau. Dispersion measurements from North Yunnan display intermediate phase velocities, higher than in the central but lower than in the outermost parts of the plateau, indicating gradual changes in the crustal thickness and shear-velocity structure from the central towards the southeastern part of Tibet (Yao *et al.* 2008; Fig. 3).

2.3 Surface wave depth sensitivity

Rayleigh and Love waves sample the Earth differently and are sensitive to different depth ranges at the same period. Fig. 4 shows Fréchet derivatives of the fundamental-mode Rayleigh and Love phase velocities with respect to shear velocity at depth, for four different periods at all of which the waves sample the thick Tibetan crust. The normalized sensitivity kernels are computed for a 1-D shear-velocity model of West Lhasa. At a 10 s period, the peak sensitivity of Rayleigh waves is at about 10 km depth; the maximum sensitivity depth and the depth span of sensitivity increases with period. Love waves are sensitive to shallower depths at the same periods. Joint inversion of broad-band, Love and Rayleigh dispersion curves can put tight constraints on isotropic-average shear speeds and radial anisotropy within the entire crust.

3 INVERSION OF PHASE-VELOCITY CURVES FOR SHEAR-VELOCITY PROFILES

Shear velocities are sensitive to temperature and composition of the rocks at depth. We invert Rayleigh- and Love-wave dispersion curves simultaneously for an isotropic average shear speed profile [$V_{S(\text{avg})} = (V_{SV} + V_{SH})/2$] and a radial anisotropy profile [$(V_{SV} - V_{SH})/2$] (Lebedev *et al.* 2006; Endrun *et al.* 2008), where V_{SV} and V_{SH} are the vertically and horizontally polarized shear speeds, respectively. The phase-velocity curves used for the inversion are resampled at a logarithmic sample spacing to balance the structural sensitivity along the broad-band curves.

3.1 Inversion set-up

The inversion is a non-linear, least square, Levenberg-Marquardt gradient search, run from MATLAB[®]. For each perturbation in the shear-speed profile, the Love- and Rayleigh-wave synthetic phase velocities are computed directly from the V_{SH} and V_{SV} models, respectively, using a suitably fast version of the MINEOS modes code (Masters, <http://geodynamics.org/cig/software/mineos>). (Errors due to the neglect of anisotropy in these calculations are around one tenth of per cent, have very weak frequency dependence, and are similar and with the same sign for the Rayleigh and Love phase velocity (Visser *et al.* 2008), with their effect thus negligible). The non-linear inversion algorithm, minimizing the data-synthetic misfit, converges to the true best-fitting solution, in the sense that no linearization is performed.

Surface wave phase velocities depend not only on V_{SV} and V_{SH} but also (although to a lesser extent) on the vertically and horizontally polarized compressional-wave velocity (V_{PV} and V_{PH}) and η (Anderson & Dziewonski 1982). These extra three parameters cannot be constrained independently from V_{SV} and V_{SH} by surface wave data alone, and controlled-source seismic experiments that could provide relevant V_P data are available only from a few profiles within the plateau. We have thus taken into account the non-negligible influence of the isotropic compressional-wave velocity [$V_{P(\text{iso})}$] on the Rayleigh-wave dispersion by varying $V_{P(\text{iso})}$ so that its ratio to the isotropic-average shear speed [$V_{S(\text{avg})}$] is constant (fixed at the value from Crust 2.0). Neglecting P -wave anisotropy may have an effect on the amplitude of S -wave anisotropy in our models. Our inferences and conclusions discussed below, however, are based on very large variations of anisotropy between regions within the plateau and thus would not be affected.

The inversion is parametrized using boxcar and triangular basis functions, each used for two independent parameters, one for the isotropic average V_S perturbation and the other for radial anisotropy. In most inversions, with the exception of those performed to test the parametrization itself (Fig. 5), the depth of the Mohorovičić discontinuity (Moho) and three intracrustal discontinuities are also inversion parameters. With 15–20 depth basis functions spanning the crust and upper mantle and mild norm damping, the inversions can fit the data closely (i.e. the numbers of parameters are sufficiently large so that the choice of a particular number does not affect the misfit) with relatively smooth, 1-D shear-velocity models.

3.2 Parametrization of the crust

The shapes of the dispersion curves at short and intermediate periods reflect the layering of shear velocity within the crust. How many parameters are necessary to capture the crustal structure? In order to determine what general structure is required by the data, we first perform an ‘overparametrized’ test inversion, with no intracrustal discontinuities but with numerous parameters for radial shear-velocity variations. Ten triangular basis functions within the crustal depth range provide ample freedom for the V_{SH} and V_{SV} models to vary so as to fit the short period data closely (Fig. 5a). Another 10 triangular basis functions are defined to parametrize the upper mantle down to the transition zone, in order to fit any anomalies required by the longer period data. The depth of the crust–mantle discontinuity is also included in the parametrization.

Fig. 5(a) shows the overparametrized test inversion for East-central Qiangtang, with the V_{SV} (blue), V_{SH} (red) and the Voigt isotropic average shear speed [$V_{S(\text{iso})} = (2V_{SV} + V_{SH})/3$] (orange) profiles plotted in the middle frame. The conspicuous reduction

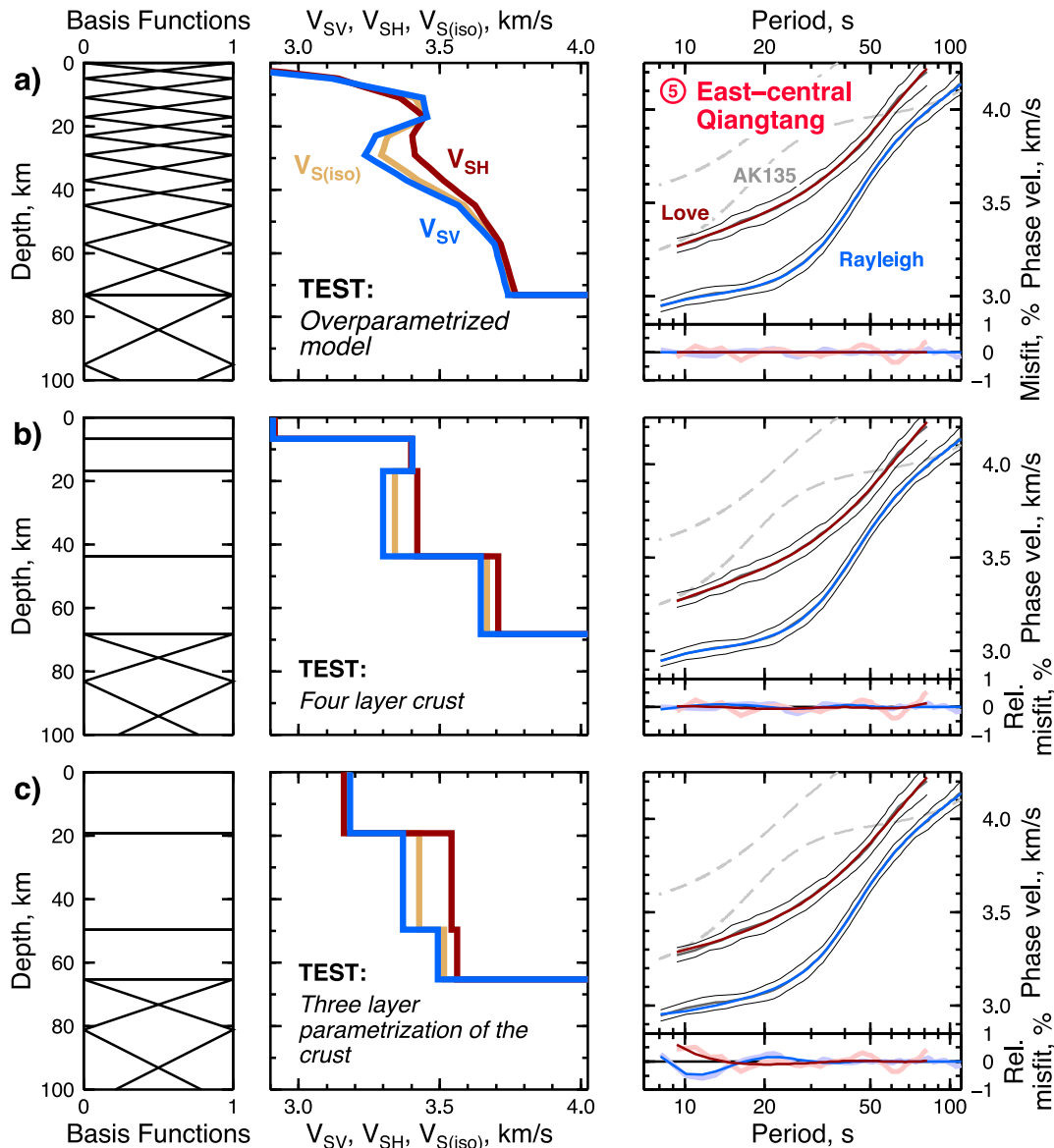


Figure 5. Three test inversions using different crustal parametrization for East-central Qiangtang. (a) An overparametrized test inversion. Left-hand side: Ten triangular basis functions parametrize the crust. Moho depth is also an inversion parameter. Centre: The best-fitting radially anisotropic S -velocity model, comprising the profiles of V_{SV} (blue), V_{SH} (red) and the Voigt isotropic average $V_{S(iso)}$ [$(2V_{SV} + V_{SH})/3$, orange]. The model does not include any intracrustal discontinuities. Right-hand side, upper frame: synthetic Rayleigh- and Love-wave dispersion curves. Dark grey curve: measured dispersion curves (hidden behind the synthetic curves). Thin black lines show the standard deviations of the data. Dashed grey curves: dispersion curves computed for AK135 (Kennett *et al.* 1995). Right-hand side, lower frame: the data-synthetic misfit for Love waves (thick pale red) and Rayleigh waves (thick pale blue). (b) Test inversion with a four-layer crust. Left-hand side: four boxcar basis functions parametrize V_S perturbations and radial anisotropy in the crust; four discontinuity parameters allow for depth changes of three intracrustal discontinuities and the Moho. Centre: best-fitting S -velocity model, depicted as in (a). Right-hand side: corresponding synthetic phase velocities and data-synthetic misfit (thick pale curves) and the misfit relative to the synthetic dispersion curves from (a) (thin bright-coloured curves). (c) Test inversion with a three-layer crust. Left-hand side: three boxcar basis functions parametrize the crust; three discontinuity parameters allow for depth changes of two intracrustal discontinuities and the Moho. Centre: best-fitting S -velocity model, shown as in (a). Right-hand side: dispersion curves and misfits, shown as in (b). All the inversions have upper mantle parametrization sufficient to fit the long period data.

in V_S between 20 and 40 km depths is required by the Rayleigh-wave phase-velocity curve, which shows a substantial decrease in its slope from 20–30 to 12–20 s (Fig. 5a, phase-velocity frame, dark grey curve behind the synthetic dispersion curve). The misfit between the synthetic dispersion curves and the data is very low for both Rayleigh and Love waves, well below ± 0.5 per cent [Fig. 5a, misfit frame, Love (pale red) and Rayleigh (pale blue)]. The remaining data-synthetic misfit is larger for Love waves and is due to noise

in the measurements. The $V_{S(iso)}$ (and V_{SV}) model in Fig. 5(a) has structure similar to that of the published V_{SV} models for northwest Himalaya (Caldwell *et al.* 2009), although somewhat faster.

The results of the overparametrized inversion show that four layers within the crust are required to fit the data: a 7–10-km thick upper crust with relatively low velocities in it, a higher-velocity upper-middle crust (around 10–20 km), a lower-middle crust with very low velocities in it (around 20–40 km), and a higher-velocity

lower crust. A test inversion for a four-layer crustal model, with four boxcar basis functions for the crust, fits the data almost as well as the overparametrized model (Fig. 5b). The four basis functions are used to parametrize the V_S perturbations and the amount of radial anisotropy within each boxcars depth range. The depth of crustal discontinuities, including the crust-mantle boundary (Moho), are also free to vary. The data-synthetic fit of the four-layer model is nearly identical to that given by the overparametrized inversion (Fig. 5b, misfit frame, pale colours), with the difference in the misfit given by the two inversions very small (Fig. 5b, misfit frame, bold colours).

A three-layer crust test inversion, in contrast, shows a substantially worse data-synthetic fit for 10–20-s periods (Fig. 5c). This demonstrates that a minimum of four crustal layers are necessary to describe the Tibetan crust.

The difference between V_{SH} and V_{SV} profiles for the same models equals radial anisotropy. Anisotropy is present in the middle and lower crust of all the three models in Fig. 5, predominantly in the mid-lower crust in the 20–45 km depth range. Joint inversion of Love- and Rayleigh-wave data allows us to determine the anisotropy and, thus, obtain the isotropic average shear speed profiles, that are directly related to temperature and composition at depth, unlike the previously published V_{SV} models which also depend on anisotropy (e.g. Caldwell *et al.* 2009; Acton *et al.* 2010; Yang *et al.* 2012; Li *et al.* 2014). The depth range of the radial anisotropy is similar to 1-D profiles presented by Shapiro *et al.* (2004), Duret *et al.* (2010) and Xie *et al.* (2013).

All our models are parametrized from the surface (0 km depth) down to the uppermost lower mantle. Topography is taken into account in the phase-velocity calculations. The reference model for each of the nine regions is determined from a two-step inversion. First, an overparametrized inversion is performed using a starting model composed of an average crustal V_S from Crust 2.0 (Bassin *et al.* 2000) and an AK135 mantle (Kennett *et al.* 1995). In the second inversion that follows, the best-fitting models are computed by perturbing an improved reference model with crustal discontinuities, Moho depth, and the average crustal V_S as determined in the first inversion, and with the mantle profile set, again, to the AK135 reference model.

3.3 Investigation of parameter ranges

The shear-velocity models yielded by the inversions are non-unique: many different models can fit the data almost equally well. Small variations in the thickness and S velocity of a layer can be compensated by changes in the velocities within and thicknesses of the layers above and below. For example, the Moho depth from the inversions of East-central Qiangtang trades off with the lower-crustal shear velocity, shallower for a low V_S and deeper for a high velocity, with little effect on the misfit for periods >40 s (Figs 5b and c).

Rather than inverting dispersion curves for a single, best-fitting S -velocity profile, we thus perform a series of gradient-search inversions, comprising multiple grid searches within specially selected parameter subspaces [similar to the model-space mapping of Bartzsch *et al.* (2011)]. These inversions are targeted to determine ranges of V_S and radial anisotropy within specific crustal depth ranges and are designed to answer questions such as: how low or how high can the shear velocity within the middle crust be, or what is the strength of the radial anisotropy within a depth range? The inversions are parametrized in a way that the property under investigation is fixed within the depth range in question, while all the

other parameters remain free to vary. Hence, the inversion takes all parameter trade-offs into account. For example, an inversion is set with a fixed V_S between 20 and 45 km depths while the other parameters, such as the V_S of the other crustal layers, Moho and the upper crustal discontinuity, as well as the anisotropy within all the layers are free to change. For each new inversion the V_S in the background model is incremented by a small step of 0.025 km s^{-1} . The data-synthetic misfits achieved in each inversion indicate which models are most consistent with the data.

This approach is different from the grid search applied by Caldwell *et al.* (2009), who performed a series of inversions by varying the V_S gradient from the surface down to 100 km depth in their different starting models, with no Moho discontinuity. Our approach also differs from Monte Carlo methods (e.g. Shapiro *et al.* 2004; Endrun *et al.* 2008; Yao *et al.* 2008, 2010; Duret *et al.* 2010; Huang *et al.* 2010; Yang *et al.* 2012; Xie *et al.* 2013), although, like them, it produces a suit of best-fitting models. The main advantage of our approach is that it explores the complete ranges of the parameters that we target, generally with no *a priori* assumptions on how broad these ranges may be (the few exceptions where we had to put prior bounds on parameter ranges are pointed out below), and that it is well suited to answer specific questions we formulate, for example regarding the range of V_S or anisotropy values within a specific depth interval. (We note that it should be possible to formulate a Monte Carlo scheme that would yield similar results.)

Fig. 6 shows the results of three test inversion series, set up to delimit: the range of shear-velocity values consistent with the data within the 20–45 km depth interval; the range of the radial anisotropy average over the same depth interval; and the range of radial anisotropy average over the entire crustal thickness. For each test we plot the Voigt isotropic average shear speed [$V_{S(\text{iso})} = (2V_{SV} + V_{SH})/3$], radial anisotropy [$V_{SH} - V_{SV}/V_{S(\text{iso})}$], the corresponding Love- and Rayleigh-wave synthetic dispersion curves, and the data-synthetic misfits. The tests for the mid-crustal shear-velocity range (left) show the expected trade-offs between shear velocities in neighbouring layers and, also, between the isotropic profile and radial anisotropy. When the S velocity between 20 and 45 km depth is set high, both the upper and lower crustal velocities decrease in the models produced by the gradient-search inversions, whilst the radial anisotropy becomes stronger so that the synthetic Rayleigh-wave phase velocity is lower, fitting the data (Fig. 6, Songpan-Ganzi). Similarly, a very low V_S within the mid-crust is compensated, to a large extent, by higher V_S in the adjacent upper and lower crustal layers and decreased radial anisotropy. The best-fitting S -velocity profile from the test series, shown in red, shows an intermediate V_S in the mid-crustal depth range and the adjacent layers. The difference between the synthetic dispersion curves corresponding to the different test models is the largest at 20–40 s periods, most sensitive to the LVZ depth range, especially for Rayleigh waves. Grey shade in the 1-D profiles shows the range of the tested values that turned out to be consistent with the data. The same approach is used to determine the ranges for mid-crustal radial anisotropy and crustal-average radial anisotropy.

The data-synthetic misfit given by the best-fitting model (Fig. 6, red curve in the misfit frame) is small, much less than 0.5 per cent at all periods. The remaining misfit is due to noise in the data.

The best-fitting models determined by the gradient-search inversions minimize the data-synthetic misfit over the entire length of the dispersion curves. While comparing the crustal structure of different models, we now compute the rms misfit over the length of the Love- and Rayleigh-wave curves up to the 60-s period only, so as to remove the contribution of the misfit at long periods, where the data

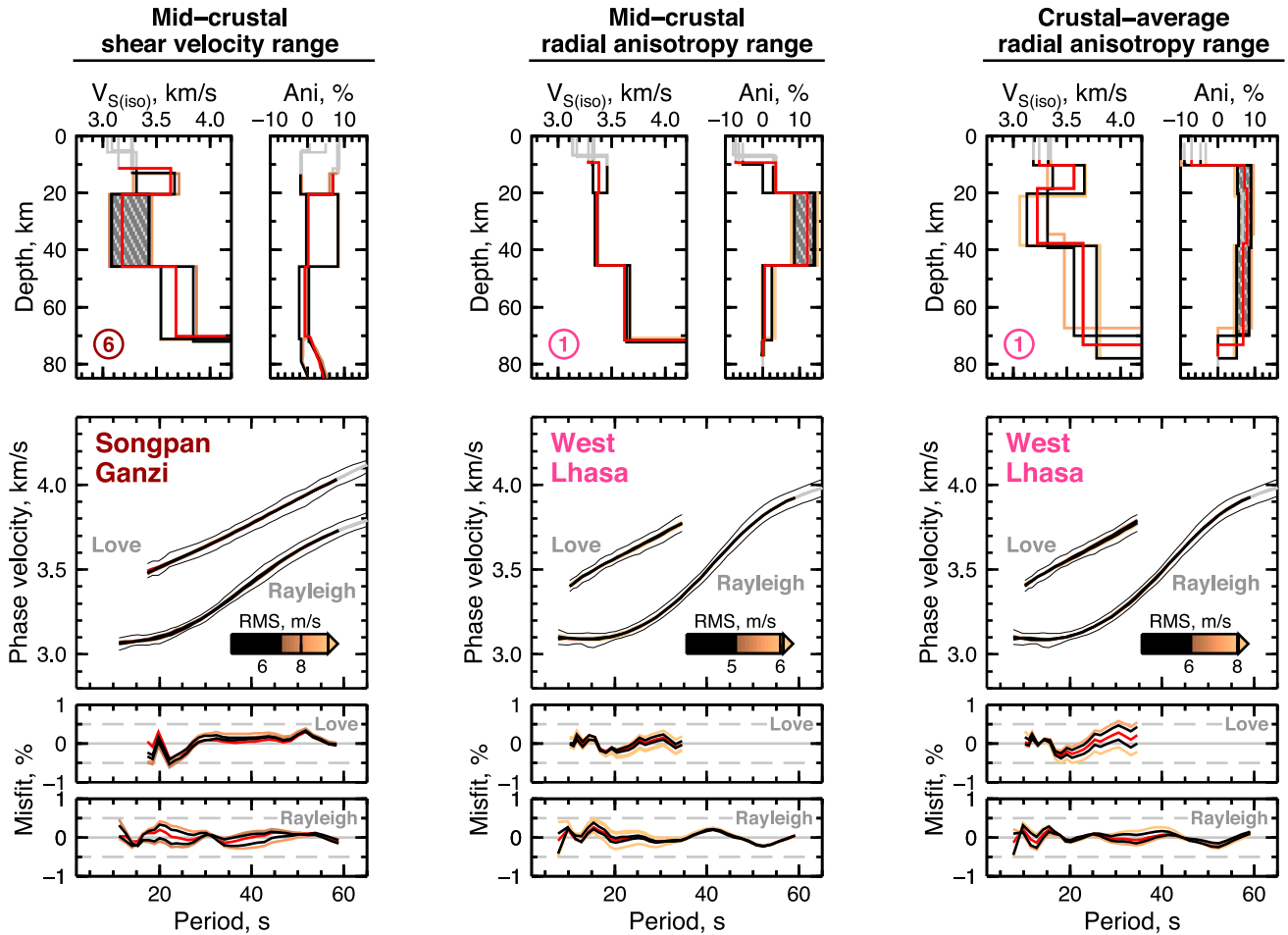


Figure 6. Grid-search test inversions performed to delimit the ranges of V_S (left-hand side) and radial anisotropy (middle) in the 20–45 km depth range, and the range for crustal-average radial anisotropy, between 10 km depth and the Moho (right-hand side). Next to the frames with the isotropic-average models [$V_{S(ISO)} = (2V_{SV} + V_{SH})/3$] are the frames with the radial anisotropy profiles [$(V_{SH} - V_{SV})/V_{S(ISO)}$]. Grey shade in the models shows the range of the tested values that turned out to be consistent with the data. Synthetic dispersion curves for each of the V_S models are plotted in the frames below. The colour scale indicates the data-synthetic rms misfit over the combined Rayleigh- and Love-wave dispersion curves, for periods up to 60 s. Black curves provide data-synthetic fits below a rms threshold. Red lines: the best-fitting models from the test series (top) and the corresponding dispersion and misfits (bottom). Thin black curves show the standard deviation of the data. The profiles are coloured in depth ranges where they are reliably constrained by the data. Left-hand side: the V_S range at 20–45 km depths beneath Songpan-Ganzi. Centre: the range for radial anisotropy at 20–45 km depths beneath West Lhasa. Right-hand side: crustal-average radial anisotropy, between 10 km depth and the Moho, West Lhasa.

are sensitive primarily to the mantle structure but often show the strongest noise, dominating the misfit functions. Parameter ranges determined in the tests are such that all the models with the parameter in question (e.g. lower-middle-crustal S velocity) within the range yield a misfit smaller than the global-minimum misfit plus a constant (2.5 m s^{-1}). The colour scale used for plotting the profiles and the corresponding dispersion curves reflects the rms misfits, with darker colours indicating smaller misfits (Fig. 6).

The shear-velocity tests for the mid-crustal LVZ of Songpan-Ganzi, 20–45 km depths, yield the lower and upper S velocity limits of 3.08 and 3.43 km s^{-1} , respectively, with a best-fitting V_S of 3.18 km s^{-1} (Fig. 6 and Table 1, Songpan-Ganzi). In this and following figures, V_S and radial anisotropy profiles are plotted in pale grey where the structure cannot be reliably resolved by the Rayleigh and Love data in the period range of the measurements.

In contrast to the Songpan-Ganzi V_S profile, the profiles for West Lhasa has no strong LVZ in isotropic-average S velocities but features, instead, strong mid-crustal radial anisotropy of ~ 10 per cent (Fig. 6, West Lhasa). Estimates of the radial anisotropy within

20–45 km depth were derived from test inversions with anisotropy fixed in this layer in the various reference models (all with $V_{SH} > V_{SV}$) and with the adjacent layers allowed to have between 0 and +3 per cent anisotropy. Thus determined mid-crustal radial anisotropy in West Lhasa has a lower and upper limits of 8.5 and 13.8 per cent, respectively. In an alternative inversion for crustal anisotropy, we did not single out the middle-crustal layer but, instead, targeted the crustal-average radial anisotropy (depth span between 10 km depth and the Moho), obtaining, for West Lhasa, a range of 5.5–8.6 per cent (Fig. 6).

The tests illustrated in Fig. 6 have been performed for all of our regions within Tibet. In an effort to identify parameter ranges that are most consistent with the data, the rms threshold factor for the crustal-average radial anisotropy tests is set to 2 m s^{-1} (above the global minimum misfit) and reduced further to 1 m s^{-1} for the mid-crustal radial anisotropy ranges. Anisotropy shows a strong trade-off with the crustal thickness, so that much of the signal of anisotropy in the data can be compensated (absorbed) by variations in crustal thickness and other parameters, in particular when the

Table 1. Shear velocity and radial anisotropy estimates for different regions within Tibet. The single values of the mid-crustal S velocities are from the best-fitting profiles. The ranges of S velocity and radial anisotropy (below) are from grid searches as illustrated in Fig. 6; all values within the ranges fit the surface wave data closely. Estimates of the radial anisotropy ranges for the middle crust (20–45 km depths) were derived from test inversions with anisotropy in the adjacent upper- and lower-crustal layers allowed to have between 0 and +3 per cent anisotropy only ($V_{SH} > V_{SV}$ being positive).

	Depth (km)	West Lhasa	West Qiangtang	Central Lhasa	S.E. Qiangtang	E.C. Qiangtang	Songpan Ganzi	North Yunnan	South Yunnan	Qinling Qilian
Region		1	2	3	4	5	6	7	8	9
Middle crust V_S (km s^{-1})	20–45	3.37	3.14	3.44	3.43	3.33	3.18	3.34	3.50	3.59
Middle crust radial anisotropy (per cent)	20–45	3.21–3.41	3.02–3.36	3.31–3.49	3.27–3.49	3.25–3.44	3.08–3.43	3.23–3.52	3.32–3.61	3.38–3.63
Crustal average radial anisotropy (per cent)	10–M	6–9	5–8	3–5	0–2	2–4	0–5	3–6	4–7	2–5

crust is relatively thin. For regions with a thinner crust (North and South Yunnan, Qinling–Qilian), we thus set the rms threshold to 1 m s^{-1} for both anisotropic tests. The selection of the rms threshold is subjective, but the reduction of the threshold value in anisotropy tests is dictated by the reduced sensitivity of the data to anisotropy in a given depth range compared to isotropic profiles, if all parameter trade-offs are taken into account: the application of the same misfit threshold in both isotropic and anisotropic tests would produce very broad anisotropic ranges for anisotropy.

A separate series of tests was performed to determine shear-velocity ranges for the lower crust. These tests were unsuccessful, due to the strong trade-offs between deep-crustal shear velocities and the Moho depth and uppermost mantle velocities. In an effort to resolve this, information on the regional Moho depth was incorporated into the inversions. The lower crustal velocities were kept below 4.0 km s^{-1} and the Moho depths were not allowed to be shallower than published depths: 70 km for Lhasa (e.g. Schulte-Pelkum *et al.* 2005; Priestley *et al.* 2008; Nábelek *et al.* 2009), 60 km for Qiangtang and Songpan–Ganzi (e.g. Zhao *et al.* 2001; Kind *et al.* 2002; Kumar *et al.* 2006; Nábelek *et al.* 2009; Tseng *et al.* 2009; Yue *et al.* 2012; Gao *et al.* 2013), 50 km in Qinling–Qilian (e.g. Liu *et al.* 2006; Shi *et al.* 2009; Karplus *et al.* 2011) and 50 km and 40 km in North and South Yunnan, respectively (e.g. Kan *et al.* 1986; Li *et al.* 2006; Xu *et al.* 2007). Nonetheless, equally well-fitting models could be obtained for lower-crustal V_S values in ranges too broad to be useful.

Plotted together, the results of all the inversions for each region characterize both the uncertainty of the shear-speed and radial-anisotropy profiles and the robust features within them. Fig. 7 shows examples of the bundles of isotropic V_S and anisotropy profiles, as well as the corresponding dispersion curves and frequency-dependent misfits, all colour-coded according to misfit. The well-fitting (dark coloured) $V_{S(\text{iso})}$ models for East-central Qiangtang have mid-crustal shear speeds between 3.2 and 3.5 km s^{-1} , with radial anisotropy in a 0–8 per cent range. The synthetic dispersion curves and data-synthetic misfits show how narrow the range of best-fitting phase-velocity curves is. Southeast Qiangtang displays mid-crustal velocities similar to East-central Qiangtang, but with probably shallower radial anisotropy. The broad ranges of lower-crustal shear speeds and the Moho depths are due to the Moho– V_S trade-off.

The formal standard errors of the measurements are much smaller than the standard deviations (plotted in our figures) and would be similar to the line thickness on the plots. This is because the formal standard errors decrease with the increasing number of measurements, under the assumption of the randomness of measurement errors, and the number of measurements that go into our phase velocity curves is very large. The (unknown) actual errors, how-

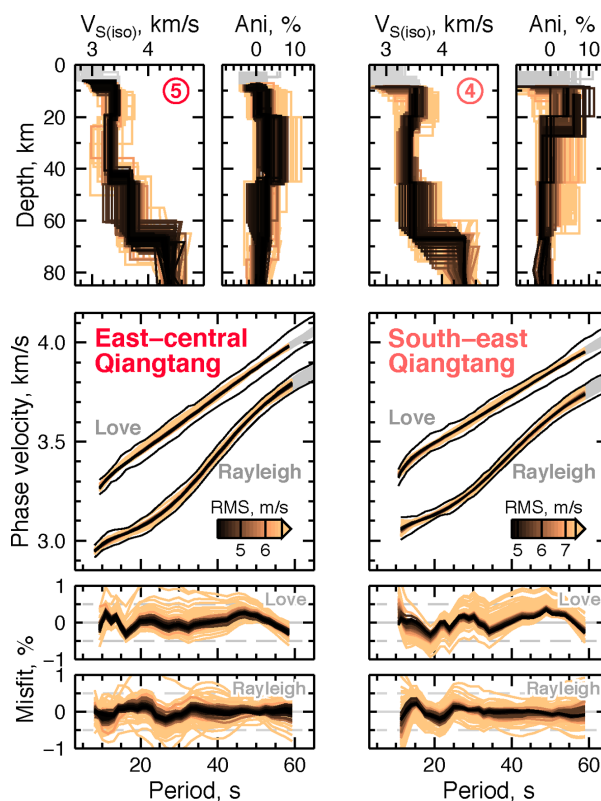


Figure 7. Bundles of radially anisotropic S -velocity profiles compiled from all the test inversions for East-central Qiangtang and Southeast Qiangtang. For each profile, the corresponding synthetic Rayleigh- and Love-wave dispersion curves and the data-synthetic misfits are plotted in the frames below, as in Fig. 6. The colour of each profile reflects the misfit. The profiles are coloured in depth ranges where they are reliably constrained by the data. All the profiles fit the data well within the standard deviation (thin black lines) at all periods. The standard errors of the measurements are much smaller than the standard deviations and would be similar to the line thickness on the plots; actual errors normally exceed standard errors because of systematic errors in the data.

ever, will normally be somewhat larger than the formal standard errors, due to the presence of systematic errors in the data.

4 RESULTS

The suites of 1-D radially anisotropic shear-velocity models for nine regions across the Tibetan Plateau are plotted in Fig. 8. For each region we show the isotropic shear-speed profiles and radial anisotropy profiles from all the test inversions. The profiles are

Shear velocity and radial anisotropy profiles

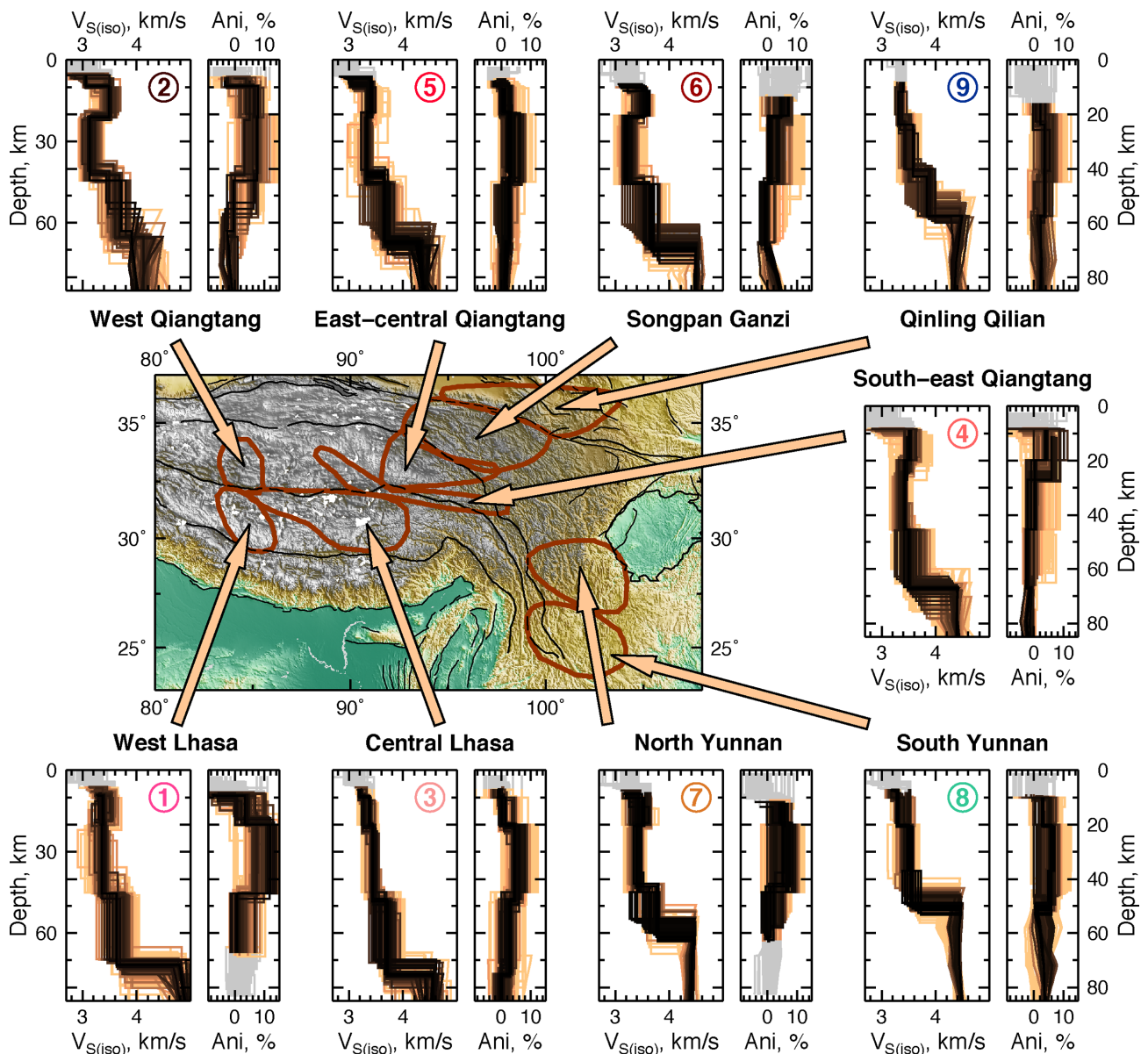


Figure 8. Bundles of radially anisotropic, S -velocity profiles compiled from all the test inversions. The models represent the average structure over the regions shown on the map (encircled brown contours; see also Fig. 3). Each individual model (each profile) is colour coded according to the data-synthetic misfit that it yields: darker colours indicate better fit. The profiles are coloured in depth ranges where they are reliably constrained by the data and are drawn light grey elsewhere.

colour-coded according to misfit, dark being the best-fitting models. The contours on the map enclose the different regions that the profiles correspond to (Fig. 3).

The plateau is characterized by low mid-crustal shear velocities ($\leq 3.5 \text{ km s}^{-1}$) across vast areas from western to southeastern Tibet, even though in Yunnan the crust thins significantly. Within the plateau, strong shear-velocity contrasts occur between different regions. Mid-crustal shear velocities decrease towards the north of the plateau: from West Lhasa (3.37 km s^{-1}) to West Qiangtang (3.14 km s^{-1}), and along the corridor from Central Lhasa to Songpan-Ganzi, from 3.44 to 3.18 km s^{-1} , respectively (Fig. 8 and Table 1). West Qiangtang, Southeast Qiangtang and Songpan-Ganzi all show a pronounced LVZ at the middle crust depths (20–45 km), with robust patterns of a decrease in shear velocity with depth be-

tween 10 and 30 km depth (Fig. 8, regions 2, 4 and 6). The contrast between the apparently monotonic velocity increase with depth in Central Lhasa and the LVZ across Songpan-Ganzi (regions 3 and 6) has been noted previously by Yang *et al.* (2012). In the case of West Lhasa, which also has no isotropic-average LVZ in the best-fitting profile (Figs 6 and 8, region 1), the strong radial anisotropy in the same depth range results in a large-amplitude LVZ in V_{SV} —as observed in previous studies (e.g. Rapine *et al.* 2003). The crustal structure and shear velocities beneath northern Yunnan are overall similar to those beneath central Tibet, including the presence of a mid-crustal LVZ, despite this region having a shallower Moho.

At the northern and southeastern margins of the plateau the crustal structure differs from that beneath the central parts of Tibet. In the north, V_S increases across the Kunlun Fault from

Songpan–Ganzi south of it (with 3.2 km s^{-1} in the middle crust) to Qinling–Qilian north of it (3.6 km s^{-1}), with the LVZ thus disappearing (regions 6 and 9). Similarly, in southern Yunnan, which shows dispersion curves very similar to those in Qinling–Qilian (Fig. 3, regions 8 and 9), the mid-crustal LVZ is absent.

Radial anisotropy within the Tibetan crust also shows strong lateral variations. The best-fitting models for West Lhasa and West Qiangtang have the strongest mid-crustal radial anisotropy, probably exceeding 9 and 5 per cent, respectively (Fig. 8, Table 1, regions 1 and 2). Radial anisotropy at the same depths but with a smaller amplitude is required by the data in Central Lhasa, East-central Qiangtang, North and South Yunnan, and Qinling–Qilian. The dispersion curves for Songpan–Ganzi and southeast Qiangtang do not require radial anisotropy in the middle and lower crust, with stronger anisotropy within shallower crust (depth less than 20 km) instead (Figs 6–8, Table 1, regions 4 and 6). The pronounced contrast in radial anisotropy between West Lhasa and Songpan–Ganzi can be seen directly in the phase velocities data (Fig. 2u and x). The Rayleigh- and Love-wave dispersion curves for West Lhasa, when compared to those for Songpan–Ganzi, diverge conspicuously between 20 and 30 s periods, sensitive to the middle crust.

In our test series, we did not target the crustal thickness specifically, keeping in mind the strong trade-off of the lower crustal shear velocities with the Moho depth, in particular for the Moho as deep as beneath Tibet (Lebedev *et al.* 2013). The Moho depth, however, was a parameter in our inversions, and we note that the crustal-thickness ranges shown by the bundles of the well-fitting profiles show meaningful variations from region to region, consistent with published Moho-depth values. The crustal thickness in the profiles is 70–80 km in southern Tibet (regions 1 and 3), 60–70 km in northern Tibet (regions 2, 4–6), 50–60 km in Qinling–Qilian (region 9), and down to about 40–50 km depth in the southeast (regions 7 and 8). These values agree with published Moho depths: a deep Moho beneath the southern Tibet (e.g. Schulte-Pelkum *et al.* 2005; Priestley *et al.* 2008; Nábelek *et al.* 2009), a shallower Moho across northern Tibet (e.g. Zhao *et al.* 2001; Kind *et al.* 2002; Kumar *et al.* 2006; Nábelek *et al.* 2009; Tseng *et al.* 2009; Yue *et al.* 2012; Gao *et al.* 2013), a sharp decrease in the crustal thickness northwards across the Kunlun Fault (Liu *et al.* 2006; Shi *et al.* 2009; Karplus *et al.* 2011), and a gradually rising Moho in southeast Tibet (Kan *et al.* 1986; Li *et al.* 2006; Xu *et al.* 2007).

5 DISCUSSION

Our models of shear wave velocity and radial anisotropy distributions within Tibetan crust yield new insight into the crustal structure, temperature, partial-melt fraction and rheology. They also prompt inferences on the mechanisms of deformation and the dynamics of the plateau.

5.1 Shear velocities within the Tibetan middle crust

Isotropic-average shear speeds within Tibetan middle crust show a systematic decrease from the south towards the north, from $\sim 3.4 \text{ km s}^{-1}$ in Lhasa to as low as $\sim 3.1\text{--}3.2 \text{ km s}^{-1}$ in West Qiangtang and eastern Songpan–Ganzi. In southeastern Tibet, where the surface elevation decreases gradually south–southeastwards, shear speeds also change gradually, increasing towards south–southeast to $\sim 3.5 \text{ km s}^{-1}$. In the northeast, our data are consistent with a sharp wave speed increase across the Kunlun Fault (Fig. 3, Table 1, Fig. 9).

Fig. 9 compares mid-crustal shear velocities constrained by our data with those from other recent models (Yao *et al.* 2008, 2010; Acton *et al.* 2010; Huang *et al.* 2010; Yang *et al.* 2012), along three north–south profiles (AA', BB' and CC') across Tibet. We find that the lateral shear-velocity variations reported in the different studies can be reconciled once anisotropy is taken into account. The isotropic V_S is notably higher than V_{SV} beneath regions with strong mid-crustal radial anisotropy such as West Lhasa and West Qiangtang. Interestingly, West Qiangtang and Songpan–Ganzi show similar, very low isotropic-average shear speeds, but the former displays strong radial anisotropy ($V_{SH} > V_{SV}$, 5 per cent minimum) and the latter does not.

Profiles AA' and BB' clearly show strong seismic-velocity variations between the different terranes (see also Table 1 and Fig. 8 for the V_S ranges, rather than values from single best-fitting models, most consistent with the data). Along profile BB' radial anisotropy decreases from south to north, with V_S and V_{SV} values thus converging beneath Songpan–Ganzi. Further north along profile BB', across the Kunlun Fault, V_S increases substantially resulting in the disappearance of the mid-crustal LVZ beneath the Qinling–Qilian Orogen. Shear velocities inferred from recent controlled-source experiments both south and north of the Kunlun Fault are significantly higher and are not plotted (Mechie *et al.* 2012); surface wave data, however, do require the very low velocities beneath the Songpan–Ganzi terrane, as confirmed by the close agreement of the results of different recent studies.

Shear velocities in the middle crust are low everywhere beneath the high plateau. An intracrustal LVZ, however—wave speeds in which are lower than both above and below—is required by the data only in the northern part of Tibet. Estimates for the LVZ amplitude from the V_S decrease between 15 and 30 km depth $[(V_{S(15)} - V_{S(30)})/V_{S(15)}]$, indicate that LVZ amplitudes vary substantially across the plateau: strongly pronounced in West Qiangtang and Songpan–Ganzi (>9 per cent V_S reduction), weaker in central and eastern Qiangtang (<3 per cent), and not required by the data across Lhasa (Fig. 11b, red shaded regions). The regional distribution of the LVZ inferred from our data broadly agrees with that displayed by the tomographic model of Yang *et al.* (2012), which shows large LVZ amplitudes (>9 per cent, V_{SV}) in northern Tibet, particularly in western Qiangtang and Songpan–Ganzi terranes. In the southern and central Tibet, the model of Yang *et al.* (2012) shows some areas with a LVZ but also large areas without it. We note that any small-scale LVZ features (Hetényi *et al.* 2011) would be averaged out in our profiles that are representative of lateral averages over a few hundred kilometres.

In a recent tomographic study using a large surface wave data set sampling eastern Tibet and surroundings, Xie *et al.* (2013) found mid-crustal shear speeds for the northeastern regions close to the upper limit of our V_S range. In an update of the model of Yang *et al.* (2012) by Hacker *et al.* (2014), the region-average shear speeds across West and Central Lhasa are similar to those in our best-fitting profiles. All the recent models display V_S decreasing towards the north for both western and eastern parts of Tibet, consistent with our results.

The crustal structure and shear velocities beneath North Yunnan are similar to those beneath central Tibet, including the mid-crustal LVZ. No LVZ is seen in South Yunnan, as in Qinling–Qilian. Along profile CC' in Fig. 9 tomography indicates strong local heterogeneity (Yao *et al.* 2008, 2010; Huang *et al.* 2010). Our profiles would average out much of any small-scale shear-velocity anomalies (Huang *et al.* 2010; Xie *et al.* 2013). The V_S structure that we determine for Yunnan agrees well with 1-D models from receiver functions for the

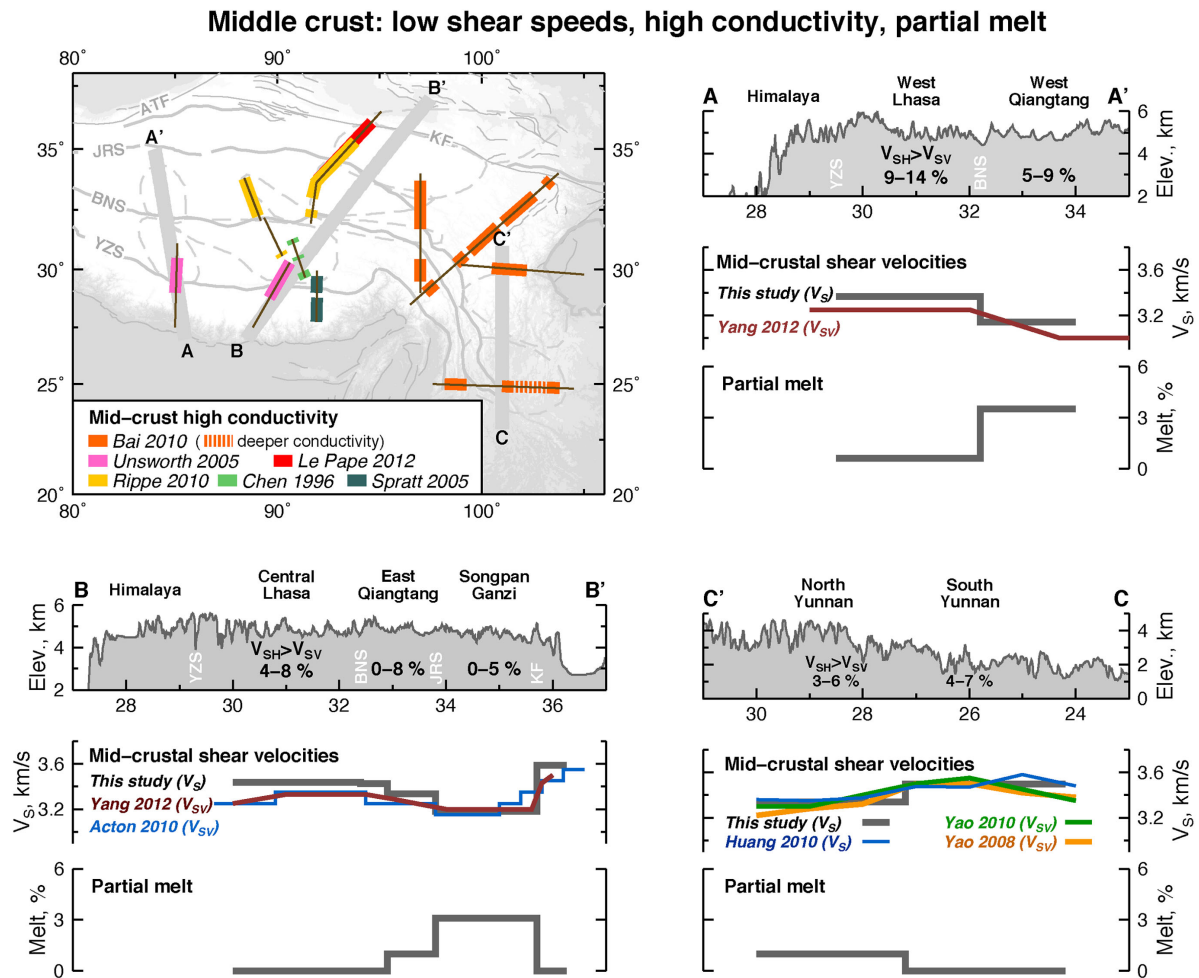


Figure 9. The middle crust beneath Tibet: shear speeds, radial anisotropy, partial melt estimates, and regions with high-conductivity areas from published magnetotelluric (MT) studies. The map shows the locations of different MT experiments (dark thin lines), the location of three cross-sections presented (thick grey lines), and the subregions sampled in this study (dashed grey lines, as in Fig. 8). Highlighted portions of the MT-profile lines indicate the regions of mid-crustal high conductivity (Chen *et al.* 1996; Spratt *et al.* 2005; Unsworth *et al.* 2005; Bai *et al.* 2010; Rippe & Unsworth 2010; Le Pape *et al.* 2012). For each cross-section, the elevation is shown along with mid-crustal average S velocities and partial melt estimates (20–45 km depth range). Our best-fitting, isotropic-average shear speeds (V_S , thick grey lines) are plotted together with shear-velocity values from other studies [coloured lines, V_{SV} : Yao *et al.* (2008, 2010); Acton *et al.* (2010); Yang *et al.* (2012) and V_S : Huang *et al.* (2010)]. The differences between velocities can be explained, in part, by mid-crustal radial anisotropy ($V_{SH} > V_{SV}$) as measured in this study, indicated in the elevation frame.

north (Xu *et al.* 2007) and south (Sun *et al.* 2014) but disagrees with tomographic models that have a three-layer crustal parametrization (Yao *et al.* 2008, 2010; Huang *et al.* 2010; Chen *et al.* 2014). These latter models either lack a distinctive LVZ or have a LVZ just above the Moho. The disagreement is probably due to the difference in the crustal configuration; a three layer crust might not have sufficient parametrization to fit the surface wave data (Fig. 5).

5.2 Temperature within the Tibetan crust

Variations in temperature and composition have a first order influence on the shear velocity of crustal rocks. Here we compare and reconcile the shear velocities we have determined with published temperature estimates for the Tibetan crust (based on seismic observations and xenoliths), using pressure- V_S -temperature relationships derived from laboratory experiments. The variations in the mid-crustal V_S are indicative of variations in thermal gradients across the plateau.

Temperature estimates at specific locations and depths beneath Tibet have been determined from the α to β quartz transition in quartz bearing rocks (Mechie *et al.* 2004). The transition gives rise to a discontinuity with a measurable seismic signature, and its detection yields a temperature estimate at a specific depth. Beneath north-central Lhasa the transition occurs at 32 km depth (0.85 GPa) and has a corresponding temperature of 800 °C (Mechie *et al.* 2004). We relate this to shear velocity at this depth and temperature using laboratory measurements and relationships. Similarly to Caldwell *et al.* (2009) and Yang *et al.* (2012), we use the laboratory measurements of Christensen (1996) performed on a variety of dry rocks at room temperature (r.t.) and at 1000 MPa (representative of pressures at 30 km depth). We select metamorphic rocks with the lowest shear velocities: metagraywacke, phyllite, granite gneiss, biotite (tonalite) gneiss, mica quartz schist and paragneulite—all in the range of 3.51–3.66 km s⁻¹, with an average of 3.62 km s⁻¹. Velocity reductions due to high temperatures are estimated by applying the V_S -temperature relationship of 2×10^{-4} km s⁻¹ per degree Celsius determined from temperature-pressure experiments on a variety of

gneisses (Kern *et al.* 2001). Thus at 800 °C the expected V_S is 3.46 km s⁻¹, close to the V_S that we have obtained for Central Lhasa (3.44 km s⁻¹) and Southeast Qiangtang (3.43 km s⁻¹), the regions beneath the INDEPTH III profile. Plutonic rocks such as granite-granodiorite have a high V_S which, at this depth and temperature, would not match the V_S for Central Lhasa.

In Qiangtang and Songpan-Ganzi, along the INDEPTH III and IV profiles, the $\alpha - \beta$ transition occurs at a shallower depth of 18 km (0.48 GPa), with a corresponding temperature of ~700 °C (Mechie *et al.* 2004, 2012). Other temperature estimates based on xenoliths from central Tibet indicate that temperatures reach 800–1000 °C at a depth of 30–50 km (0.8–1.3 GPa; Hacker *et al.* 2000). At these temperatures the calculated shear velocity for hot solid rocks, including pelitic rocks (Hacker *et al.* 2000), is still above 3.4 km s⁻¹ (Hacker *et al.* 2014), much higher than the V_S across west and central Qiangtang and Songpan-Ganzi.

Laboratory experiments show that following the $\alpha - \beta$ transition, further increase in temperature continues to decrease S velocities at a higher rate, followed by a rapid decrease at the onset of partial melting (e.g. Mueller & Massonne 2001). The melting temperatures of muscovite-rich rocks are in the range of 750–950 °C at 1.0–1.6 GPa (e.g. Clemens & Vielzeuf 1987; Patiño Douce & Harris 1998; Patiño Douce & McCarthy 1998; Litvinovsky *et al.* 2000; Holyoke & Rushmer 2002). Assuming the composition of mica-bearing crustal rocks and temperatures of >800 °C, partial melting is thus likely to occur, reducing shear velocities substantially (Hacker *et al.* 2014).

Mid-crustal temperatures of about ~800 °C can account for the low shear velocities in Central Lhasa, Southeast Qiangtang and South Yunnan. In regions with the lowest mid-crustal velocities, in particular in northern Tibet (West Qiangtang and Songpan-Ganzi), temperatures are higher and probably exceed melting temperatures, with the partial melting required to account for the very low V_S .

5.3 Partial melting in the Tibetan crust

5.3.1 Partial melt estimates from shear wave speeds

Shear wave velocities in western and northern Tibet are lower than those expected for hot solid rocks. This is consistent with previously published estimates of temperature, exceeding the solidus, and adds to the convincing evidence for partial melting in Tibetan crust. Melts can be either dry or wet; in the former rocks are molten due to high temperature exceeding the ‘dry solidus’, and in the latter rocks contain small amounts of water that lower the melting temperature (‘wet solidus’). Note that shear velocities alone cannot distinguish between a dry or wet partially molten rock, nonetheless the partial-melt estimates yield useful information regarding the rheology of the rocks (e.g. Rosenberg & Handy 2005).

Here we derive two estimates for the amount of partial melt beneath different parts of Tibet. One is based on the assumption that the V_S^0 of solid crustal rocks equals the velocity in the upper-middle crust just above the LVZ (similar to the approach adopted by Caldwell *et al.* 2009). The other estimate is based on how much lower V_S in the LVZ is compared to the reference V_S^0 of 3.4 km s⁻¹—a velocity well below the expected V_S of hot dry solid rocks at 30 km depth (a conservative approach also applied by Yang *et al.* 2012). Mid-crustal V_S/V_S^0 ratios are converted into the melt fraction using an analytical relationship between small fluid fractions of silicate melts and seismic-velocity reductions (Watanabe 1993, Fig. 10). These relationships are similar to those yielded by other V_S -melt

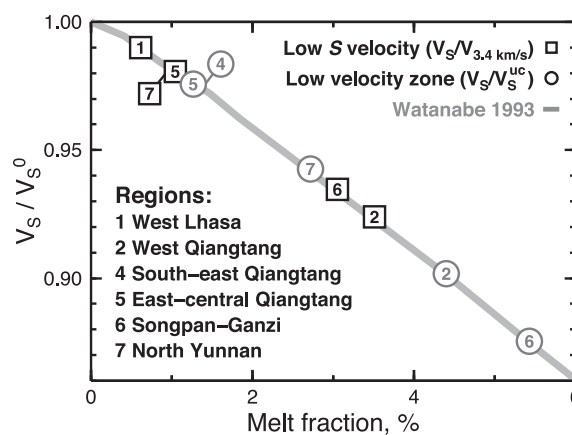


Figure 10. Mid-crustal partial melt estimates for different regions across the plateau. Estimates are based on the analytical shear velocity relationship of V_S/V_S^0 and rock fluid fractions by Watanabe (1993) (light grey curve). V_S is the velocity within the mid-crustal (30 km depth), according to the best-fitting, region-average profile. Black squares: Partial melt estimates using a reference S velocity of crustal rocks on the onset of melting at 30 km depth, $V_S^0 = 3.4$ km s⁻¹ (see text for details). Grey circles: Partial melt estimates based on the decrease in velocity compared to that in the layer above the LVZ (V_S^0). The symbols are plotted only for the regions beneath which partial melting is required, according to the criterion.

experiments (Takei 2000) and theoretical calculations (Taylor & Singh 2002), as also illustrated by Caldwell *et al.* (2009).

Our estimates for mid-crustal partial melt fractions are completely dependent on shear velocities and hence have a distribution similar to that of low S velocities. Percentages of melt derived from best-fitting profiles show that West Qiangtang and Songpan-Ganzi have melt fractions between 3 and 6 per cent, whereas North Yunnan, eastern Qiangtang and West Lhasa have melts less than 3, 2 and 1 per cent, respectively (Fig. 10). Central Lhasa, South Yunnan and Qinling-Qilian are unlikely to have any significant volume of melt. The two different definitions we adopt for melt estimates yield similar distributions of partial melting and show a correlation between the melt percentage and the LVZ amplitude (Fig. 11b).

Our partial melt values for eastern Qiangtang are consistent with the ≤ 2 per cent melt estimated by Hacker *et al.* (2014). Our values for West Qiangtang and Songpan-Ganzi are within the range of melt estimates for northwest Himalaya from 1-D V_{SV} seismic models (2.5–7 per cent, Caldwell *et al.* 2009). Finally, our estimates for North Yunnan are consistent with the ≤ 4 per cent suggested by Xu *et al.* (2007).

The very low (or nil) partial melt fractions suggested by our data across southcentral Tibet are also consistent with other published geophysical observations. Unlike southernmost Tibet, along INDEPTH I and II profiles where a thin layer of aqueous fluids has been inferred from magnetotelluric studies (Li *et al.* 2003) and seismic ‘bright spots’ (Makovsky & Klemperer 1999), central Lhasa and south-central Qiangtang terranes, along the INDEPTH III profile, show high resistivity (INDEPTH 500 line, Rippe & Unsworth 2010) and no seismic ‘bright spots’ (Haines *et al.* 2003).

5.3.2 Partial melt estimates from electrical resistivity

Magnetotelluric studies of Tibet’s crust have detected a drop in electrical resistivity at about 20 km depth in a number of locations. The resistivity (or its inverse, the electrical conductivity) of the rocks

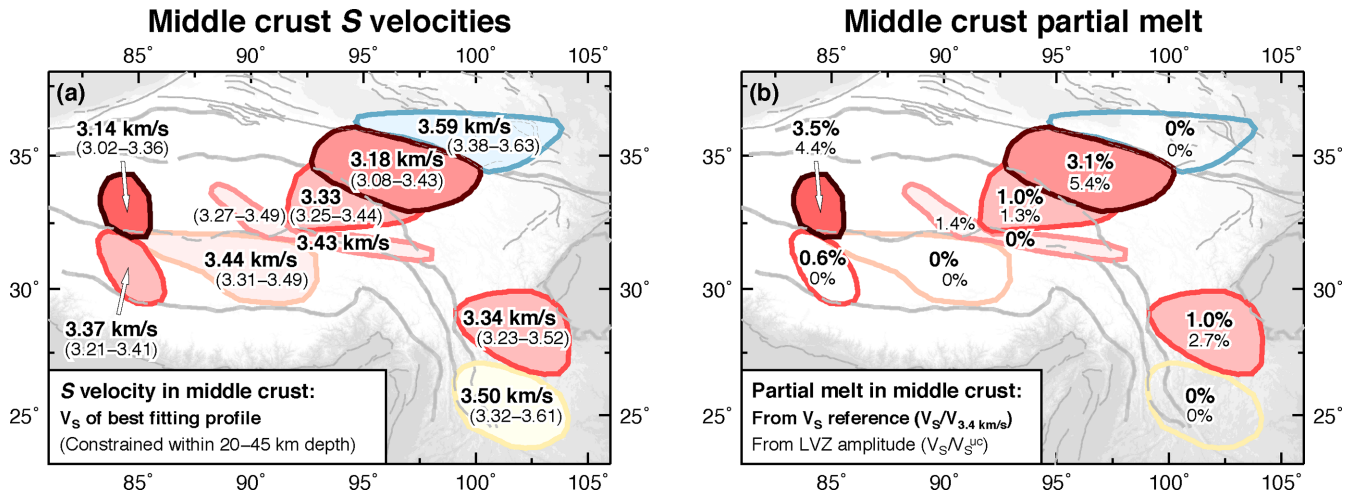


Figure 11. Summary maps of mid-crustal shear velocities, low-velocity zones and estimated partial melt. (a) Best-fitting, isotropic-average S velocities (bold) and V_S ranges for the middle crust in the 20–45 km depth range (in parentheses) (Table 1). Background colour also corresponds to mid-crustal V_S , from the lowest (dark red) to the highest (blue). (b) Estimates of mid-crustal partial melt based on the analytical relationship of V_S/V_S^0 and rock fluid fractions by Watanabe (1993) (Fig. 10). Values in bold font: Partial-melt estimates from best fitting shear velocity and a reference S velocity of 3.4 km s^{-1} for hot solid rocks. Values in light font: Partial-melt estimates from the decrease in V_S from the layer above the LVZ. Red shaded regions indicate areas where a mid-crustal LVZ is required by the data.

can be influenced by high temperatures, melts, hydrous minerals or a combination of all. Mid-crustal conductivity is not the same across the entire plateau and varies even within the same terranes (Fig. 9). Between 20 and 45 km depths, very high conductivity is mapped just north of the Himalayas and in southern Lhasa (Chen *et al.* 1996; Spratt *et al.* 2005; Unsworth *et al.* 2005), with sparser observations in Central Lhasa (Chen *et al.* 1996; Rippe & Unsworth 2010). High conductivity has also been reported beneath northern Qiangtang (Rippe & Unsworth 2010), beneath Songpan-Ganzi up to the Kunlun Fault (Bai *et al.* 2010; Le Pape *et al.* 2012), and in southeastern Tibet (Bai *et al.* 2010). The distribution of conductivity broadly agrees with that of low mid-crustal shear velocities not only in terms of depth, but also with the north–south pattern of decreasing V_S and increasing conductivity, from Central Lhasa towards northern Tibet up to the Kunlun Fault. East-central Qiangtang, Songpan-Ganzi and North Yunnan are all characterized by high conductivity, low V_S , a LVZ, and, therefore, high likelihood of substantial partial melt. In contrast, regions with relatively high V_S , no LVZ, and, thus, with no melt required by seismic data, have intermittent or no high-conductivity zones; these include West and Central Lhasa, Southeast Qiangtang, Qinling-Qilian and South Yunnan. [The latter region appears to display high conductivity at a greater depth, below 40 km depth (Bai *et al.* 2010).]

Estimates of fluid content from electrical conductivity cover a broad range. MT studies typically estimate the conductance of a layer, with a strong trade-off between conductivity within and the thickness of the partially molten layer (Li *et al.* 2003). In addition, aqueous fluids could produce the same conductance with a lower fluid fraction and/or a lesser layer thickness. Li *et al.* (2003) proposes that a layer of 10–15 per cent aqueous fluid a few hundred metres thick overlying a thick layer of partial melt gives the most consistent explanation to both the MT and seismic data for the Himalayas and southern Lhasa. Melt estimates based on MT observations include 2–4 per cent melt for the Himalaya and 5–14 per cent for southern Lhasa (Unsworth *et al.* 2005), 2–6 per cent for northern Tibet (Unsworth *et al.* 2004) and 5–20 per cent across southeast Tibet (Bai *et al.* 2010). Melt estimates based on shear velocities are normally at the lower end of the ranges based on MT. A

joint analysis of shear velocities and conductivity for melt estimates remains desirable.

5.3.3 Variations in partial melting across Tibet

In summary, a variety of geophysical observations indicate partial melting within Tibetan crust, with a melt fraction that varies across the plateau. Fluids within the crust can be either partial melt or aqueous (e.g. saline fluids). Across the Himalayas, partial melt is inferred from bright spots in seismic reflection data (Brown *et al.* 1996; Makovsky *et al.* 1996) and high conductivity (Pham *et al.* 1986; Unsworth *et al.* 2005), possibly with a thin layer of aqueous fluid on top (Makovsky & Klemperer 1999; Li *et al.* 2003). Wet melts here can be a result of dehydration associated with eclogitization reaction in the lower crust (Hetényi *et al.* 2007). Wide-spread fluids are unlikely across Central Lhasa and south-central Qiangtang terranes, as evident from the lack of seismic ‘bright spots’ (Haines *et al.* 2003), high resistivity (Rippe & Unsworth 2010), low-to-normal Poisson’s ratio (Owens & Zandt 1997) and moderately low shear velocities (this study). In northern Tibet, partial melting is likely to be with a relatively large melt fraction but dry, as has been inferred from the absence of the seismic bright spots (Haines *et al.* 2003), high temperature and absence of hydrous minerals (Hacker *et al.* 2000), high conductivity (e.g. Unsworth *et al.* 2004; Le Pape *et al.* 2012), low S velocities (this study, Yang *et al.* 2012) and high Poisson’s ratio (Owens & Zandt 1997). [The Poisson ratio for Songpan-Ganzi using our S velocity and a V_P of 6.25 km s^{-1} (Karplus *et al.* 2011) is 0.33 or, V_P/V_S of 1.96.] Crustal radiogenic heating (McKenzie & Priestley 2008) and heating from the asthenosphere below a warm, thin mantle lithosphere (e.g. Barron & Priestley 2009; Ceylan *et al.* 2012; Agius & Lebedev 2013; Nunn *et al.* 2013) are likely to be the main causes for the elevated temperature, low V_S and melts in the crust of northern Tibet.

The very low seismic velocities in the middle crust beneath Tibet indicate that it is mechanically weak and prone to ductile flow. In northern Tibet, the occurrence of mid-crustal seismic LVZ suggests that the middle crust is a particularly weak layer there.

Laboratory experiments by Rosenberg & Handy (2005) show that as little as 5 per cent of melt can drop viscosity by an order of magnitude. This could facilitate channel flow beneath the Tibetan Plateau as simulated by numerical models (e.g. Royden 1997; Clark & Royden 2000). Similar models have been used to explain high-grade metamorphic rocks exhumed at the Greater Himalayan Sequence (Beaumont *et al.* 2001; Jamieson *et al.* 2004). A viscosity drop at mid-crustal depths has been proposed based on partial melt estimates from seismic (Caldwell *et al.* 2009) and MT (Unsworth *et al.* 2005) studies. Estimates for viscosity and flow rate by Rippe & Unsworth (2010) suggest that eastern Tibet has a lower viscosity than northern Lhasa and Qiangtang (central Tibet). This is consistent with the distributions of low shear velocities and partial melt that we have obtained from our surface wave data (Fig. 11).

5.4 Radial anisotropy

Radial seismic anisotropy (the difference of the speeds of vertically and horizontally polarized seismic waves) indicates preferred alignment of anisotropic minerals within the Earth, created by large finite strains. In the top ~5 km of the crust, anisotropy can also be caused by aligned microcracks opened by tectonic stress (e.g. Adam & Lebedev 2012), but at the greater depths that we focus on here the cracks close and anisotropy is primarily due to the anisotropic fabric, created in the last major episode of crustal deformation. Given the pervasive active deformation of Tibet, anisotropy in its ductile middle crust can be interpreted with confidence as a proxy for current and recent deformation. Strong radial anisotropy has been detected in Tibetan crust in a number of previous studies (Shapiro *et al.* 2004; Chen *et al.* 2009; Duret *et al.* 2010; Guo *et al.* 2012; Xie *et al.* 2013). One of the targets of our inversions was to constrain the amplitude of radial anisotropy in different parts of the plateau.

We constrained the ranges of crustal radial anisotropy consistent with surface wave data in two series of inversions, one targeting the average anisotropy from 20 to 45 km depth and the other from 10 km depth to the Moho (Fig. 6). Beneath Lhasa, West Qiangtang and Qingling-Qilian radial anisotropy is clearly the strongest in the middle crust (20–45 km depth; Fig. 8). Among the regions sampled by our data, mid-crustal radial anisotropy is the strongest in West Lhasa (9–14 per cent, $V_{SH} > V_{SV}$). In other regions, East-central Qiangtang and Yunnan, radial anisotropy is either less pronounced or harder to constrain within the mid-crust only. Hence, tests for crustal-average radial anisotropy were introduced. These give tighter ranges of values (Figs 6 and 12c, Table 1).

The regional variations of radial anisotropy that we map (Figs 8 and 12) are overall consistent with those given by the regional tomography of Shapiro *et al.* (2004), including the weak (or absent) radial anisotropy in northeastern Tibet. The recent tomography model of Xie *et al.* (2013) also shows a decrease in radial anisotropy from west to east, although with stronger positive anisotropy in eastern Tibet, close to the upper limit of our anisotropy ranges. Strong radial anisotropy variations from west to east Tibet are also seen in the update of the model of Yang *et al.* (2012), by Hacker *et al.* (2014). The 1-D models of Duret *et al.* (2010), for paths crossing the entire plateau from west to east, confirm the occurrence of substantial anisotropy and probably show averages of very strong radial anisotropy in western Tibet and weaker anisotropy in eastern Tibet.

Shapiro *et al.* (2004) pointed out an important relationship between the distributions of radial anisotropy in the deep crust and the style of deformation seen at the surface. Anisotropy is strong

beneath western and central Tibet, characterized by normal faulting and, thus, crustal thinning, and weak (or absent) in the east and northeast where the deformation is primarily strike-slip, with no overall crustal thinning. Shapiro *et al.* (2004) inferred that as much as 30 per cent of vertical thinning of the middle-to-lower crust was required to account for the anisotropy (probably caused by a horizontal alignment of mica crystals) in western-central Tibet.

Lateral variations of radial anisotropy constrained by our data confirm the relationship between anisotropy and the style of deformation identified by Shapiro *et al.* (2004). In Fig. 12 we compare the distribution of radial anisotropy to surface elevation, faults of different types (predominantly normal faults in the western-central part of Tibet; strike-slip faults in eastern and northeastern Tibet, and thrust faults at the periphery), and earthquake source mechanisms (confirming the regional variations of the deformation style).

Strong radial anisotropy correlates neither with highest surface elevation, nor with low shear velocities (and, by inference, partial melting and low viscosity regions; Fig. 11). For example, West Lhasa and West Qiangtang regions both show strong radial anisotropy but mid-crustal shear velocities are quite different. Central Lhasa and North Yunnan regions display significant radial anisotropy but different elevations. Instead, the radial anisotropy shows a relationship with the surface deformation, shown by the different fault types across the plateau and the focal mechanism of upper crustal earthquakes (Figs 12a–c). Strong radial anisotropy is observed in regions experiencing crustal extension (flattening) in west-central Tibet and southeast Tibet, whereas regions experiencing strike-slip deformation display no (or much weaker) radial anisotropy (Fig. 12d). Radial anisotropy is also detected in the northern margins of the plateau, beneath regions experiencing crustal thickening (e.g. Yuan *et al.* 2013).

Strong mid-crustal radial anisotropy would be consistent with deformation of a mechanically weak layer that flows as if confined to a channel (e.g. Bird 1991; Royden 1997; Clark & Royden 2000). The middle-to-lower crust could probably flow to escape from beneath western-central Tibet. Just as anisotropic crystals can become nearly horizontally oriented as a result of ongoing vertical thinning in western-central Tibet, strike-slip-style flow may align micas in a vertical or steeply dipping plane, resulting in weaker radial anisotropy—as observed across Songpan-Ganzi.

5.5 Deformation and dynamics of the Tibetan crust

Our observations provide new constraints on the structure and temperature of Tibetan crust, on the distribution of partial melt within it and on the patterns of its deformation. These results prompt useful inferences on the basic mechanisms of the plateau's dynamics.

The main direct cause of the deformation of the Tibetan crust is gravity—the gravitational spreading of the very thick crust. Compression and addition of new crustal material from the south, over tens of millions of years, are the underlying cause, as they are the reason for the crustal thickening. The evolution of topography, crustal thickness, and crustal deformation must also have been affected by flow within the crust and by the dynamics of mantle lithosphere, although the nature of the flow within both the crust and upper mantle beneath Tibet is debated (e.g. England & Houseman 1989; Clark & Royden 2000; Hatzfeld & Molnar 2010; Clark 2012; Wang *et al.* 2012a; Agius & Lebedev 2014).

Geodetic measurements map the kinematics at the surface in detail and show overall eastward movement of Tibetan crust away from the western-central Tibet (Zhang *et al.* 2004; Gan *et al.* 2007),

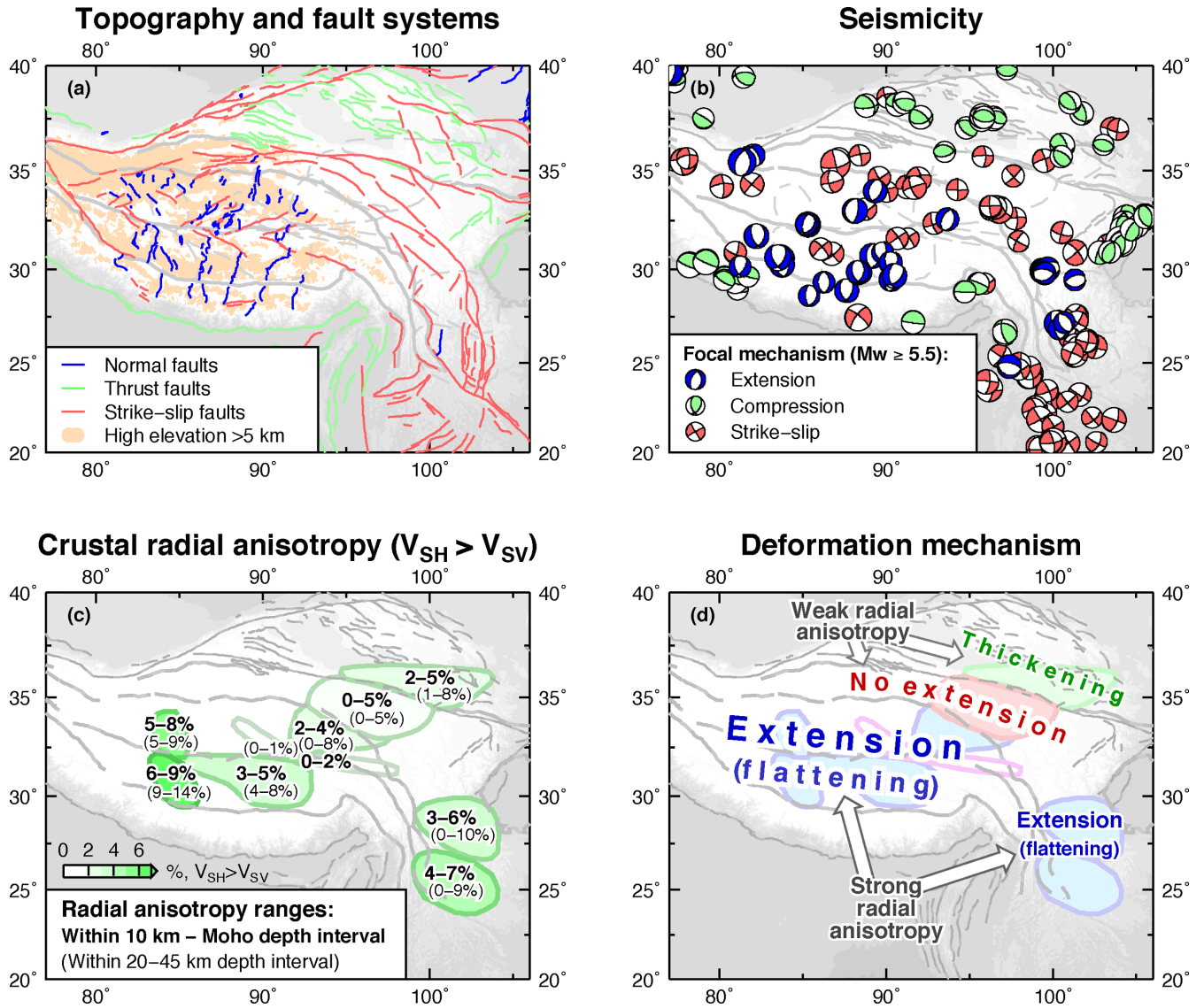


Figure 12. Deformation and radial anisotropy in the Tibetan crust. (a) Different fault systems colour-coded according to their type (normal, thrust, and strike-slip) from Taylor & Yin (2009). Orange shade highlights regions of elevation higher than 5 km (using ETOPO1 elevation data set, re-sampled at 5 km × 5 km grid by GMT, Wessel & Smith 1998). Thick grey lines indicate sutures, dashed grey loops indicate regions. (b) Focal mechanism of shallow earthquakes (<50 km depth) with moment magnitude ≥ 5.5 . The focal mechanisms are well-constrained double couple CMT solutions (<http://www.globalcmt.org>), colour-coded according to their type (extension, compression, and strike-slip). (c) Ranges of crustal-average radial anisotropy [$(V_{SH} - V_{SV})/V_{S(iso)}$], between 10 km depth and the Moho (bold, black numbers), and ranges of radial anisotropy in the 20–45 km depth range (light, black numbers in parentheses). (d) The relationship of the deformation regime and radial anisotropy within Tibetan crust.

where the elevation is the highest. The boundary conditions include the presence of nearly rigid lithospheric blocks of surrounding cratons, the main ones being India in the south, Tarim in the northwest, and Yangtze in the east. Mountain ranges form at the boundaries of Tibet and these cratonic blocks, but the flow of crustal material is blocked at the craton boundaries. Instead, Tibetan crust escapes into areas with mechanically weak lithosphere, most notably in the southeast (Yunnan).

Insights into the nature of the movements within the deep crust can be gained from seismic structure and anisotropy. The flow may, first, depend on the viscosity of crustal rocks (characterizing their response to pressure gradients). Very low shear speeds generally indicate low viscosity of rocks within the crust. The lowest shear velocities are found in the middle crust beneath northern and western Tibet, as noted previously by Yang *et al.* (2012) and confirmed

in this study. Crustal temperature varies laterally across the plateau, increasing from the south to the north. In northern Tibet, crustal radiogenic heating (McKenzie & Priestley 2008) as well as heating from the asthenosphere below the thin, warm lithosphere are probably the causes for the high temperature and low shear velocities. In the south, Lhasa is also expected to have crustal radiogenic sources, but, in contrast to northern Tibet, the cold Indian lithosphere underthrust beneath it (e.g. Ni & Barazangi 1984; Agius & Lebedev 2013) insulates the crust, to some extent, from heating from below. Furthermore, the likely presence of recently added, cold Indian crustal rocks may also contribute to the lower temperature (and, thus, higher S velocity) in southern compared to northern Tibet. We note that in the west of the plateau the zone of lowest S velocity is relatively close to the Himalaya, closer than the central parts of Tibet underlain by higher V_S middle crust. We speculate that the

northeastward flow in the deep crust, similar to that mapped by geodetic measurements at the surface, may be moving the colder crustal rocks from southern to central and eastern Tibet. At the same time, the hotter rocks in the northwest of the plateau remain roughly where they are, continue to be heated radiogenically and are not cooled by recently added Indian crustal rocks. Clearly, the patterns of flow within Tibetan crust may have a major influence on the distribution of its temperature; they remain a first-order, open question.

The lateral variations in crustal shear wave speeds and radial anisotropy show no correlation (Figs 11 and 12). This suggests that the variations in viscosity across the plateau do not determine the patterns of flow. The western-central part of the plateau that shows extension at the surface and strong radial anisotropy in the middle crust comprises a western portion with very low shear speeds (and, probably, very low viscosity) and an eastern portion with moderately low shear speeds (and, thus, higher viscosity).

Our results also provide evidence for smooth variations in the crustal structure across broad regions within Tibet. The dispersion curves measured at different station pairs within the same regions are remarkably similar, indicating relatively homogeneous structure across them (e.g. Songpan-Ganzi; Fig. 2).

5.6 Layered versus vertically coherent deformation

The distributions of radial anisotropy within the crust and the upper mantle beneath Tibet do not correlate. Anisotropy in the mantle, measured recently using broad-band surface wave data (Agius & Lebedev 2013), is stronger beneath Songpan-Ganzi (3–9 per cent) than beneath Qiangtang, in contrast to the pattern in the crust (Fig. 12). The upper-mantle radial anisotropy measurements (Agius & Lebedev 2013) are probably dominated by the fabric in the asthenosphere, which, therefore, deforms differently from the lithosphere. Shear wave splitting, often used as a source of constraints on deformation at depth (e.g. Flesch *et al.* 2005; Wang *et al.* 2008), is thus likely to occur in multiple layers with different deformation and anisotropy within each (Agius 2013; Agius & Lebedev 2014).

6 CONCLUSIONS

The Tibetan middle crust is characterized by anomalously low shear wave speeds. The wave speeds also show substantial lateral variations across the plateau. In the central Lhasa Terrane, shear speeds in the middle crust (20–45 km depth range) are around 3.4 km s^{-1} . The lowest mid-crustal shear speeds are found in the north and west of the plateau, down to as low as $3.1\text{--}3.2 \text{ km s}^{-1}$ in West Qiangtang and eastern Songpan-Ganzi. In these regions, a pronounced mid-crustal LVZ (with shear speeds in the middle crust lower than those in the upper crust above it) is required by the data. In southeastern Tibet, crustal shear wave speeds increase gradually towards southeast (from 3.3 to 3.5 km s^{-1}). In the northeast, crustal wave speeds are markedly higher to the north of Kunlun Fault (around 3.6 km s^{-1}) than to the south of it (around 3.2 km s^{-1} ; Fig. 11(a)).

The lateral variations of shear speeds within the crust are indicative of those in temperature. Across Lhasa, at mid-crustal depth, a temperature of $800 \text{ }^\circ\text{C}$ (Mechie *et al.* 2004) is sufficient to explain the shear speeds there (about 3.4 km s^{-1}). Regions with S velocities similar to or higher than these (Southeast Qiangtang, South Yunnan) probably have similar or lower mid-crustal temperatures. Farther north, across West Qiangtang and Songpan-Ganzi, the ther-

mal gradient is steeper than in the south and the temperature at mid-crustal depths exceeds the solidus, resulting in partial melting that lowers the shear speed further (e.g. Hacker *et al.* 2014).

Our conservative partial melt estimates yield between 3 and 6 per cent melt fractions for West Qiangtang and Songpan-Ganzi, respectively, and melt fractions less than 3, 2 and 1 per cent for North Yunnan, eastern Qiangtang and West Lhasa, respectively (Fig. 11b). In South Yunnan, significant melting is unlikely. Beneath Tibet's margins, the crust is thinner and shear speeds within it are higher, reflecting its lower temperature.

The top of the low shear velocity zone within the Tibetan crust ($\sim 20 \text{ km}$ depth) coincides with the top of a high conductivity layer, detected in magnetotelluric studies. Northern Tibet is characterized by a pronounced LVZ and high conductivity. In contrast, in southern Tibet (across Lhasa), a LVZ is not required by the data, and electrical conductivity is low or laterally varying. Melt estimates based on V_S are at the lower end of melt estimates inferred in published magnetotelluric studies.

Strong radial anisotropy is required by the data in western-central Tibet (>5 per cent) but not in northeastern Tibet (Fig. 12c). The amplitude of radial anisotropy in the crust does not correlate with how low isotropic-average shear speeds are (and, thus, with partial melt fractions and low viscosities) or with surface elevation. Instead, radial anisotropy is related to the deformation pattern and is the strongest in regions experiencing extension (crustal flattening; Fig. 12). Crustal thinning causes the radial anisotropy probably by aligning mica crystals in the horizontal plane (Shapiro *et al.* 2004). Strike-slip type of deformation may, instead, align micas in a vertical or steeply dipping plane, resulting in weaker radial anisotropy, as observed in eastern Songpan-Ganzi, a region experiencing strike-slip earthquakes and no overall extension. Interestingly, the strength of radial anisotropy within the crust and the upper mantle beneath Tibet (Agius & Lebedev 2013) do not correlate, with the anisotropy in the mantle stronger in northeastern than in west-central Tibet, in contrast to the pattern in the crust. This suggests that the deformation in the crust and the upper $\sim 100 \text{ km}$ of the mantle is significantly different.

The close similarity of dispersion curves at neighbouring station pairs suggests that the crust is largely uniform beneath broad regions within Tibet (hundreds of kilometres wide). Thus, deformation and flow in the middle crust are likely to be diffuse and distributed smoothly over broad areas, consistent with the low topographic gradients within Tibet (Clark & Royden 2000).

The growth of Tibet by the addition of Indian crustal rocks into its crust from the south is reflected in the higher crustal seismic velocities (and, thus, lower temperatures) in the southern compared to northern parts of the plateau. This is because more recently added rocks have had less time to undergo radioactive heating within the thickened Tibetan crust. Gravity-driven flattening is the basic cause of extension and normal faulting in the southern, western and central Tibet, as evidenced by pervasive radial anisotropy in the middle crust beneath the regions undergoing extension. The overall flow of the crust is directed towards the east by the boundaries and by the motions of the lithospheric blocks that surround Tibet.

ACKNOWLEDGEMENTS

The authors would like to thank Peter Molnar, an anonymous reviewer and the Editor, Michael Ritzwoller, for detailed, constructive reviews that helped us to improve this paper. The facilities of the IRIS Data Management System (IRIS Data Management Center)

were used for access to waveform and metadata used in this study. Figures were made using Generic Mapping Tools (GMT) software (Wessel & Smith 1998). This study was supported by Science Foundation Ireland (grants 08/RFP/GEO1704 and 09/RFP/GEO2550).

REFERENCES

- Acton, C.E., Priestley, K., Gaur, V.K. & Rai, S.S., 2010. Group velocity tomography of the Indo-Eurasian collision zone, *J. geophys. Res.*, **115**(B12), 1–16.
- Adam, J.M.-C. & Lebedev, S., 2012. Azimuthal anisotropy beneath southern Africa from very broad-band surface-wave dispersion measurements, *Geophys. J. Int.*, **191**(1), 155–174.
- Agius, M.R., 2013. The structure and dynamics of the lithosphere beneath Tibet from seismic surface-wave analysis, *PhD thesis*, Trinity College Dublin.
- Agius, M.R. & Lebedev, S., 2013. Tibetan and Indian lithospheres in the upper mantle beneath Tibet: evidence from broadband surface-wave dispersion, *Geochem. Geophys. Geosyst.*, **14**(10), 4260–4281.
- Agius, M.R. & Lebedev, S., 2014. Multi-layered azimuthal anisotropy beneath Tibet, constrained by broadband Rayleigh-wave dispersion, in *Proceedings of the EGU General Assembly, Geophysical Research Abstracts*, EGU2014-16689, Vol. 16.
- Anderson, D.L. & Dziewonski, A.M., 1982. Upper mantle anisotropy: evidence from free oscillations, *Geophys. J. Int.*, **69**(2), 383–404.
- Armijo, R., Tapponnier, P., Mercier, J.L. & Han, T.-L., 1986. Quaternary extension in southern Tibet: field observations and tectonic implications, *J. geophys. Res.*, **91**(B14), 13 803–13 872.
- Arora, B.R., Unsworth, M.J. & Rawat, G., 2007. Deep resistivity structure of the northwest Indian Himalaya and its tectonic implications, *Geophys. Res. Lett.*, **34**(4), 1–4.
- Bai, D. *et al.*, 2010. Crustal deformation of the eastern Tibetan Plateau revealed by magnetotelluric imaging, *Nat. Geosci.*, **3**(5), 358–362.
- Barron, J. & Priestley, K., 2009. Observations of frequency-dependent Sn propagation in Northern Tibet, *Geophys. J. Int.*, **179**(1), 475–488.
- Bartzsch, S., Lebedev, S. & Meier, T., 2011. Resolving the lithosphere-asthenosphere boundary with seismic Rayleigh waves, *Geophys. J. Int.*, **186**(3), 1152–1164.
- Bassin, C., Laske, G. & Masters, G., 2000. The current limits of resolution for surface wave tomography in North America, *EOS, Trans. Am. geophys. Un.*, **81**, F897.
- Beaumont, C., Jamieson, R.A., Nguyen, M.H. & Lee, B., 2001. Himalayan tectonics explained by extrusion of a low-viscosity crustal channel coupled to focused surface denudation, *Nature*, **414**(6865), 738–742.
- Bird, P., 1991. Lateral Extrusion of Lower Crust From Under High Topography in the Isostatic Limit, *J. geophys. Res.*, **96**(B6), 10 275–10 286.
- Brown, L.D. *et al.*, 1996. Bright spots, structure, and magmatism in southern Tibet from INDEPTH seismic reflection profiling, *Science*, **274**(5293), 1688–1690.
- Caldwell, W.B., Klemperer, S.L., Rai, S.S. & Lawrence, J.F., 2009. Partial melt in the upper-middle crust of the northwest Himalaya revealed by Rayleigh wave dispersion, *Tectonophysics*, **477**(1–2), 58–65.
- Ceylan, S., Ni, J., Chen, J.Y., Zhang, Q., Tilmann, F. & Sandvol, E., 2012. Fragmented Indian plate and vertically coherent deformation beneath eastern Tibet, *J. geophys. Res.*, **117**(B11), B11303, doi:10.1029/2012JB009210.
- Chen, L., Booker, J.R., Jones, A.G., Wu, N., Unsworth, M.J., Wei, W. & Tan, H., 1996. Electrically conductive crust in southern Tibet from INDEPTH magnetotelluric surveying, *Science*, **274**(5293), 1694–1696.
- Chen, M., Huang, H., Yao, H., van der Hilst, R. & Niu, F., 2014. Low wave speed zones in the crust beneath SE Tibet revealed by ambient noise adjoint tomography, *Geophys. Res. Lett.*, **41**(2), 334–340.
- Chen, Y., Badal, J. & Zhang, Z., 2009. Radial anisotropy in the crust and upper mantle beneath the Qinghai-Tibet Plateau and surrounding regions, *J. Asian Earth Sci.*, **36**(4–5), 289–302.
- Christensen, N.I., 1996. Poisson's ratio and crustal seismology, *J. geophys. Res.*, **101**(B2), 3139–3156.
- Chun, K.-Y. & Yoshii, T., 1977. Crustal structure of the Tibetan Plateau: a surface-wave study by a moving window analysis, *Bull. seism. Soc. Am.*, **67**(3), 735–750.
- Clark, M.K., 2012. Continental collision slowing due to viscous mantle lithosphere rather than topography, *Nature*, **483**(7387), 74–77.
- Clark, M.K. & Royden, L.H., 2000. Topographic ooze: building the eastern margin of Tibet by lower crustal flow, *Geology*, **28**(8), 703–706.
- Clemens, J. & Vielzeuf, D., 1987. Constraints on melting and magma production in the crust, *Earth planet. Sci. Lett.*, **86**(2–4), 287–306.
- Cotte, N., Pedersen, H., Campillo, M., Mars, J., Ni, J.F., Kind, R., Sandvol, E. & Zhao, W., 1999. Determination of the crustal structure in southern Tibet by dispersion and amplitude analysis of Rayleigh waves, *Geophys. J. Int.*, **138**(3), 809–819.
- de Vos, D., Paulssen, H. & Fichtner, A., 2013. Finite-frequency sensitivity kernels for two-station surface wave measurements, *Geophys. J. Int.*, **194**(2), 1042–1049.
- Duret, F., Shapiro, N.M., Cao, Z., Levin, V., Molnar, P. & Roecker, S., 2010. Surface wave dispersion across Tibet: direct evidence for radial anisotropy in the crust, *Geophys. Res. Lett.*, **37**(16), 1–5.
- Dziewonski, A.M., Ekström, G. & Salganik, M.P., 1994. Centroid-moment tensor solutions for January–March 1994, *Phys. Earth planet. Inter.*, **86**(4), 253–261.
- Elliott, J.R., Walters, R.J., England, P.C., Jackson, J.A., Li, Z. & Parsons, B., 2010. Extension on the Tibetan Plateau: recent normal faulting measured by INSAR and body wave seismology, *Geophys. J. Int.*, **183**(2), 503–535.
- Endrun, B., Meier, T., Lebedev, S., Bohnhoff, M., Stavrakakis, G. & Harjes, H.-p., 2008. S velocity structure and radial anisotropy in the Aegean region from surface wave dispersion, *Geophys. J. Int.*, **174**(2), 593–616.
- England, P. & Houseman, G., 1989. Extension during continental convergence, with application to the Tibetan plateau, *J. geophys. Res.*, **94**(B12), 17 561–17 579.
- Fielding, E., Isacks, B., Barazangi, M. & Duncan, C., 1994. How flat is Tibet?, *Geology*, **22**(2), 163–167.
- Flesch, L.M., Holt, W.E., Silver, P.G., Stephenson, M., Wang, C.-Y. & Chan, W.W., 2005. Constraining the extent of crust-mantle coupling in central Asia using GPS, geologic, and shear wave splitting data, *Earth planet. Sci. Lett.*, **238**(1–2), 248–268.
- Fullea, J., Lebedev, S., Agius, M.R., Jones, A.G. & Afonso, J.C., 2012. Lithospheric structure in the Baikal-central Mongolia region from integrated geophysical-petrological inversion of surface-wave data and topographic elevation, *Geochem. Geophys. Geosyst.*, **13**(1), doi:10.1029/2012GC004138.
- Gan, W., Zhang, P., Shen, Z.-K., Niu, Z., Wang, M., Wan, Y., Zhou, D. & Cheng, J., 2007. Present-day crustal motion within the Tibetan Plateau inferred from GPS measurements, *J. geophys. Res.*, **112**(B8), 1–14.
- Gao, R., Chen, C., Lu, Z., Brown, L.D., Xiong, X., Li, W. & Deng, G., 2013. New constraints on crustal structure and Moho topography in Central Tibet revealed by SinoProbe deep seismic reflection profiling, *Tectonophysics*, **606**, 160–170.
- Guo, Z., Gao, X., Yao, H., Li, J. & Wang, W., 2009. Midcrustal low-velocity layer beneath the central Himalaya and southern Tibet revealed by ambient noise array tomography, *Geochem. Geophys. Geosyst.*, **10**(5), doi:10.1029/2009GC002458.
- Guo, Z., Gao, X., Wang, W. & Yao, Z., 2012. Upper- and mid-crustal radial anisotropy beneath the central Himalaya and southern Tibet from seismic ambient noise tomography, *Geophys. J. Int.*, **189**(2), 1169–1182.
- Hacker, B.R., Gnos, E., Ratschbacher, L., Grove, M., McWilliams, M., Sobolev, S.V., Wan, J. & Zhenhan, W., 2000. Hot and dry deep crustal xenoliths from Tibet, *Science*, **287**(5462), 2463–2466.
- Hacker, B.R., Ritzwoller, M.H. & Xie, J., 2014. Partially melted, mica-bearing crust in Central Tibet, *Tectonics*, **33**, 1408–1424.
- Haines, S.S., Klemperer, S.L., Brown, L., Jingru, G., Mechie, J., Meissner, R., Ross, A. & Wenjin, Z., 2003. INDEPTH III seismic data: from surface observations to deep crustal processes in Tibet, *Tectonics*, **22**(1), doi:10.1029/2009RG000304.
- Hatzfeld, D. & Molnar, P., 2010. Comparisons of the kinematics and deep structures of the Zagros and Himalaya and of the Iranian and Tibetan Plateaus and geodynamic implications, *Rev. Geophys.*, **48**(2), 1–48.

- Hetényi, G., Cattin, R., Brunet, F., Bollinger, L., Vergne, J., Nábělek, J.L. & Diament, M., 2007. Density distribution of the India plate beneath the Tibetan Plateau: geophysical and petrological constraints on the kinetics of lower-crustal eclogitization, *Earth planet. Sci. Lett.*, **264**(1-2), 226–244.
- Hetényi, G., Vergne, J., Bollinger, L. & Cattin, R., 2011. Discontinuous low-velocity zones in southern Tibet question the viability of the channel flow model, in *Growth and Collapse of the Tibetan Plateau*, Vol. 353, pp. 99–108, eds Gloaguen, R. & Ratschbacher, L., Geol. Soc. Lond.
- Holyoke, C.W. & Rushmer, T., 2002. An experimental study of grain scale melt segregation mechanisms in two common crustal rock types, *J. Metamorph. Geol.*, **20**(5), 493–512.
- Huang, H., Yao, H. & van der Hilst, R.D., 2010. Radial anisotropy in the crust of SE Tibet and SW China from ambient noise interferometry, *Geophys. Res. Lett.*, **37**(21), 1–5.
- Huang, W.-C. *et al.*, 2000. Seismic polarization anisotropy beneath the central Tibetan Plateau, *J. geophys. Res.*, **105**(B12), 27 979–27 989.
- Huang, Z., Peng, Y., Luo, Y., Zheng, Y. & Wei, S., 2004. Azimuthal anisotropy of Rayleigh waves in East Asia, *Geophys. Res. Lett.*, **31**(15), 1–4.
- Jamieson, R.A., Beaumont, C., Medvedev, S. & Nguyen, M.H., 2004. Crustal channel flows: 2. Numerical models with implications for metamorphism in the Himalayan-Tibetan Orogen, *J. geophys. Res.*, **109**(B6), 1–24.
- Kan, R.J., Hu, H.X., Zeng, R.S., Mooney, W.D. & McEvilly, T.V., 1986. Crustal Structure of Yunnan Province, People's Republic of China, from seismic refraction profiles, *Science*, **234**(4775), 433–437.
- Kapp, P. & Guynn, J.H., 2004. Indian punch rifts Tibet, *Geology*, **32**(11), 993–996.
- Karplus, M.S., Zhao, W., Klemperer, S.L., Wu, Z., Mechie, J., Shi, D., Brown, L.D. & Chen, C., 2011. Injection of Tibetan crust beneath the south Qaidam Basin: evidence from INDEPTH IV wide-angle seismic data, *J. geophys. Res.*, **116**(B7), 1–23.
- Karplus, M.S., Klemperer, S.L., Lawrence, J.F., Zhao, W., Mechie, J., Tilmann, F., Sandvol, E. & Ni, J., 2013. Ambient-noise tomography of north Tibet limits geological terrane signature to upper-middle crust, *Geophys. Res. Lett.*, **40**(5), 808–813.
- Kennett, B. L.N., Engdahl, E.R. & Buland, R., 1995. Constraints on seismic velocities in the Earth from traveltimes, *Geophys. J. Int.*, **122**(1), 108–124.
- Kern, H., Popp, T., Gorbatshev, F., Zharikov, A., Lobanov, K. & Smirnov, Y., 2001. Pressure and temperature dependence of VP and VS in rocks from the superdeep well and from surface analogues at Kola and the nature of velocity anisotropy, *Tectonophysics*, **338**(2), 113–134.
- Kind, R. *et al.*, 1996. Evidence from earthquake data for a partially molten crustal layer in Southern Tibet, *Science*, **274**(5293), 1692–1694.
- Kind, R. *et al.*, 2002. Seismic images of crust and upper mantle beneath Tibet: evidence for Eurasian plate subduction, *Science*, **298**(5596), 1219–1221.
- Klemperer, S., 2006. Crustal flow in Tibet: geophysical evidence for the physical state of Tibetan lithosphere, and inferred patterns of active flow, *Geol. Soc., Lond., Spec.*, **268**, 39–70.
- Kumar, P., Yuan, X., Kind, R. & Ni, J., 2006. Imaging the colliding Indian and Asian lithospheric plates beneath Tibet, *J. geophys. Res.*, **111**(B6), 1–11.
- Le Pape, F., Jones, A.G., Vozar, J. & Wenbo, W., 2012. Penetration of crustal melt beyond the Kunlun Fault into northern Tibet, *Nature*, **5**(5), 330–335.
- Lebedev, S. & van der Hilst, R.D., 2008. Global upper-mantle tomography with the automated multimode inversion of surface and S-wave forms, *Geophys. J. Int.*, **173**(2), 505–518.
- Lebedev, S., Nolet, G., Meier, T. & van der Hilst, R.D., 2005. Automated multimode inversion of surface and S waveforms, *Geophys. J. Int.*, **162**(3), 951–964.
- Lebedev, S., Meier, T. & van der Hilst, R.D., 2006. Asthenospheric flow and origin of volcanism in the Baikal Rift area, *Earth planet. Sci. Lett.*, **249**(3-4), 415–424.
- Lebedev, S., Adam, J.M.-C. & Meier, T., 2013. Mapping the Moho with seismic surface waves: a review, resolution analysis, and recommended inversion strategies, *Tectonophysics*, **609**, 377–394.
- Lev, E., Long, M.D. & van der Hilst, R.D., 2006. Seismic anisotropy in Eastern Tibet from shear wave splitting reveals changes in lithospheric deformation, *Earth planet. Sci. Lett.*, **251**(3-4), 293–304.
- Li, H., Shen, Y., Huang, Z., Li, X., Gong, M., Shi, D., Sandvol, E. & Li, A., 2014. The distribution of the mid-to-lower crustal low-velocity zone beneath the northeastern Tibetan Plateau revealed from ambient noise tomography, *J. geophys. Res.*, **119**(3), 1954–1970.
- Li, L., Li, A., Shen, Y., Sandvol, E.A., Shi, D., Li, H. & Li, X., 2013. Shear wave structure in the northeastern Tibetan Plateau from Rayleigh wave tomography, *J. geophys. Res.*, **118**(8), 4170–4183.
- Li, S., Unsworth, M.J., Booker, J.R., Wei, W., Tan, H. & Jones, A.G., 2003. Partial melt or aqueous fluid in the mid-crust of Southern Tibet? Constraints from INDEPTH magnetotelluric data, *Geophys. J. Int.*, **153**(2), 289–304.
- Li, S., Mooney, W.D. & Fan, J., 2006. Crustal structure of mainland China from deep seismic sounding data, *Tectonophysics*, **420**, 239–252.
- Litvinovsky, B.A., Steele, I.M. & Wickham, S.M., 2000. Silicic Magma Formation in Overthickened Crust: melting of Charnockite and Leucogranite at 15, 20 and 25 kbar, *J. Petrol.*, **41**(5), 717–737.
- Liu, M., Mooney, W.D., Li, S., Okaya, N. & Detweiler, S., 2006. Crustal structure of the northeastern margin of the Tibetan Plateau from the Songpan-Ganzi terrane to the Ordos basin, *Tectonophysics*, **420**(1–2), 253–266.
- Makovsky, Y. & Klemperer, S.L., 1999. Measuring the seismic properties of Tibetan bright spots: evidence for free aqueous fluids in the Tibetan middle crust, *J. geophys. Res.*, **104**(B5), 10 795–10 825.
- Makovsky, Y., Klemperer, S.L., Ratschbacher, L., Brown, L.D., Li, M., Zhao, W. & Meng, F., 1996. INDEPTH wide-angle reflection observation of P-wave-to-S-wave conversion from crustal bright spots in Tibet, *Science*, **274**(5293), 1690–1691.
- McKenzie, D. & Priestley, K., 2008. The influence of lithospheric thickness variations on continental evolution, *Lithos*, **102**(1–2), 1–11.
- Mechie, J. *et al.*, 2004. Precise temperature estimation in the Tibetan crust from seismic detection of the α - β quartz transition, *Geology*, **32**(7), 601–604.
- Mechie, J. *et al.*, 2012. Crustal shear (S) velocity and Poisson's ratio structure along the INDEPTH IV profile in northeast Tibet as derived from wide-angle seismic data, *Geophys. J. Int.*, **191**, 369–384.
- Meier, T., Dietrich, K., Stöckhert, B. & Harjes, H.-P., 2004. One-dimensional models of shear wave velocity for the eastern Mediterranean obtained from the inversion of Rayleigh wave phase velocities and tectonic implications, *Geophys. J. Int.*, **156**(1), 45–58.
- Molnar, P. & Tapponnier, P., 1975. Cenozoic Tectonics of Asia: effects of a continental collision, *Science*, **189**(4201), 419–426.
- Mueller, H.J. & Massonne, H.J., 2001. Experimental high pressure investigation of partial melting in natural rocks and their influence on Vp and Vs, *Phys. Chem. Earth Pt. A*, **26**(4–5), 325–332.
- Nábělek, J., Vergene, J. & Hetenyi, G., 2005. Project Hi-CLIMB: a synoptic view of the Himalayan collision zone and Southern Tibet, in *AGU Fall Meeting Abstracts*, pp. T52A–02.
- Nábelek, J. *et al.*, 2009. Underplating in the Himalaya-Tibet collision zone revealed by the Hi-CLIMB experiment, *Science*, **325**(5946), 1371–1374.
- Nelson, K.D. *et al.*, 1996. Partially molten middle crust beneath Southern Tibet: synthesis of project INDEPTH results, *Science*, **274**(5293), 1684–1688.
- Ni, J. & Barazangi, M., 1984. Seismotectonics of the Himalayan collision zone: geometry of the underthrusting Indian plate beneath the Himalaya, *J. geophys. Res.*, **89**(B2), 1147–1163.
- Nunn, C. *et al.*, 2013. Imaging the lithosphere beneath NE Tibet: teleseismic P and S body wave tomography incorporating surface wave starting models, *Geophys. J. Int.*, **196**(3), 1724–1741.
- Owens, T.J. & Zandt, G., 1997. Implications of crustal property variations for models of Tibetan Plateau evolution, *Nature*, **387**(6628), 37–43.
- Owens, T.J., Randall, G.E., Wu, F.T. & Zeng, R., 1993. PASSCAL instrument performance during the Tibetan Plateau passive seismic experiment, *Bull. seism. Soc. Am.*, **83**, 1959–1970.
- Patiño Douce, A.E. & Harris, N., 1998. Experimental constraints on Himalayan anatexis, *J. Petrol.*, **39**(4), 689–710.

- Patiño Douce, A.E. & McCarthy, T.C., 1998. Melting of crustal rocks during continental collision and subduction, in *When Continents Collide: Geodynamics and Geochemistry of Ultrahigh-Pressure Rocks*, Chap. 2, pp. 27–55, eds Hacker, B.R. & Liou, J.G., Kluwer Academic.
- Pham, V.N., Boyer, D., Therme, P., Yuan, X.C., Li, L. & Jin, G.Y., 1986. Partial melting zones in the crust in southern Tibet from magnetotelluric results, *Nature*, **319**(6051), 310–314.
- Priestley, K., Debayle, E., McKenzie, D. & Piliidou, S., 2006. Upper mantle structure of eastern Asia from multimode surface waveform tomography, *J. geophys. Res.*, **111**(B10), doi:10.1029/2005JB004082.
- Priestley, K., Jackson, J. & McKenzie, D., 2008. Lithospheric structure and deep earthquakes beneath India, the Himalaya and southern Tibet, *Geophys. J. Int.*, **172**(1), 345–362.
- Rapine, R., Tilmann, F., West, M., Ni, J. & Rodgers, A., 2003. Crustal structure of northern and southern Tibet from surface wave dispersion analysis, *J. geophys. Res.*, **108**(B2), doi:10.1029/2001JB000445.
- Replumaz, A., Negrodo, A.M., Guillot, S., der Beek, P.V. & Villaseñor, A., 2010. Crustal mass budget and recycling during the India/Asia collision, *Tectonophysics*, **492**(1–4), 99–107.
- Rippe, D. & Unsworth, M., 2010. Quantifying crustal flow in Tibet with magnetotelluric data, *Phys. Earth planet. Inter.*, **179**(3–4), 107–121.
- Romanowicz, B.A., 1982. Constraints on the structure of the Tibet Plateau from pure path phase velocities of Love and Rayleigh waves, *J. geophys. Res.*, **87**(B8), 6865–6883.
- Rosenberg, C.L. & Handy, M.R., 2005. Experimental deformation of partially melted granite revisited: implications for the continental crust, *J. Metamor. Geol.*, **23**(1), 19–28.
- Royden, L.H., 1997. Surface deformation and lower crustal flow in Eastern Tibet, *Science*, **276**(5313), 788–790.
- Royden, L.H., Burchfiel, B.C. & van der Hilst, R.D., 2008. The geological evolution of the Tibetan Plateau, *Science*, **321**(5892), 1054–1058.
- Schaeffer, A. & Lebedev, S., 2013. Global shear speed structure of the upper mantle and transition zone, *Geophys. J. Int.*, **194**(1), 417–449.
- Schulte-Pelkum, V., Monsalve, G., Sheehan, A., Pandey, M.R., Sapkota, S., Bilham, R. & Wu, F., 2005. Imaging the Indian subcontinent beneath the Himalaya, *Nature*, **435**(7046), 1222–1225.
- Searle, M.P., Elliott, J.R., Phillips, R.J. & Chung, S.-L., 2011. Crustal-lithospheric structure and continental extrusion of Tibet, *J. Geol. Soc.*, **168**(3), 633–672.
- Shapiro, N.M., Ritzwoller, M.H., Molnar, P. & Levin, V., 2004. Thinning and flow of Tibetan crust constrained by seismic anisotropy, *Science*, **305**(5681), 233–236.
- Shi, D., Shen, Y., Zhao, W. & Li, A., 2009. Seismic evidence for a Moho offset and south-directed thrust at the easternmost Qaidam-Kunlun boundary in the Northeast Tibetan Plateau, *Earth planet. Sci. Lett.*, **288**(1–2), 329–334.
- Sol, S. *et al.*, 2007. Geodynamics of the southeastern Tibetan Plateau from seismic anisotropy and geodesy, *Geology*, **35**(6), 563–566.
- Spratt, J.E., Jones, A.G., Nelson, K.D. & Unsworth, M.J., 2005. Crustal structure of the India-Asia collision zone, southern Tibet, from INDEPTH MT investigations, *Phys. Earth planet. Inter.*, **150**(1–3), 227–237.
- Su, W., Wang, C. & Huang, Z., 2008. Azimuthal anisotropy of Rayleigh waves beneath the Tibetan Plateau and adjacent areas, *Sci. China Ser. D-Earth Sci.*, **51**(12), 1717–1725.
- Sun, X. *et al.*, 2014. Crustal structure beneath SE Tibet from joint analysis of receiver functions and Rayleigh wave dispersion, *Geophys. Res. Lett.*, **41**(5), 1479–1484.
- Takei, Y., 2000. Acoustic properties of partially molten media studied on a simple binary system with a controllable dihedral angle, *J. geophys. Res.*, **105**(B7), 16 665–16 682.
- Taylor, M. & Yin, A., 2009. Active structures of the Himalayan-Tibetan Orogen and their relationships to earthquake distribution, contemporary strain field, and Cenozoic volcanism, *Geosphere*, **5**(3), 199–214.
- Taylor, M.A.J. & Singh, S.C., 2002. Composition and microstructure of magma bodies from effective medium theory, *Geophys. J. Int.*, **149**(1), 15–21.
- Tseng, T.L., Chen, W.P. & Nowack, R.L., 2009. Northward thinning of Tibetan crust revealed by virtual seismic profiles, *Geophys. Res. Lett.*, **36**(24), doi:10.1029/2009GL040457.
- Unsworth, M. *et al.*, 2004. Crustal and upper mantle structure of northern Tibet imaged with magnetotelluric data, *J. geophys. Res.*, **109**(B2), 1–18.
- Unsworth, M.J. *et al.*, 2005. Crustal rheology of the Himalaya and Southern Tibet inferred from magnetotelluric data, *Nature*, **438**(7064), 78–81.
- Visser, K., Trampert, J., Lebedev, S. & Kennett, B., 2008. Probability of radial anisotropy in the deep mantle, *Earth planet. Sci. Lett.*, **270**(3), 241–250.
- Wang, C.-y., Flesch, L.M., Silver, P.G., Chang, L.-J. & Chan, W.W., 2008. Evidence for mechanically coupled lithosphere in central Asia and resulting implications, *Geology*, **36**(5), 363–366.
- Wang, E., Kirby, E., Furlong, K.P., Van Soest, M., Xu, G., Shi, X., Kamp, P.J. & Hodges, K., 2012a. Two-phase growth of high topography in eastern Tibet during the Cenozoic, *Nat. Geosci.*, **5**(9), 640–645.
- Wang, Q. *et al.*, 2012b. Crustal melting and flow beneath northern Tibet: evidence from mid-Miocene to Quaternary strongly peraluminous rhyolites in the southern Kunlun range, *J. Petrol.*, **53**(12), 2523–2566.
- Watanabe, T., 1993. Effects of water and melt on seismic velocities and their application to characterization of seismic reflectors, *Geophys. Res. Lett.*, **20**(24), 2933–2936.
- Wei, W. *et al.*, 2001. Detection of widespread fluids in the Tibetan crust by magnetotelluric studies, *Science*, **292**(5517), 716–718.
- Wessel, P. & Smith, W.H.F., 1998. New, improved version of generic mapping tools released, *EOS, Trans. Am. geophys. Un.*, **79**(47), 579–579.
- Xie, J., Ritzwoller, M.H., Shen, W., Yang, Y., Zheng, Y. & Zhou, L., 2013. Crustal radial anisotropy across Eastern Tibet and the Western Yangtze Craton, *J. geophys. Res.*, **118**(8), 4226–4252.
- Xu, L., Rondenay, S. & van der Hilst, R.D., 2007. Structure of the crust beneath the southeastern Tibetan Plateau from teleseismic receiver functions, *Phys. Earth planet. Inter.*, **165**(3–4), 176–193.
- Yang, Y., Zheng, Y. & Ritzwoller, M.H., 2010. Rayleigh-wave phase velocities and azimuthal anisotropy in Tibet and surrounding regions from ambient noise tomography, in *Proceedings of the 25th Himalaya-Karakoram-Tibet Workshop*, U.S. Geological Survey, Open-File Report 2010-1099.
- Yang, Y., Ritzwoller, M.H., Zheng, Y., Shen, W., Levshin, A.L. & Xie, Z., 2012. A synoptic view of the distribution and connectivity of the mid-crustal low velocity zone beneath Tibet, *J. geophys. Res.*, **117**(B4), 1–20.
- Yao, H., Beghein, C. & van der Hilst, R.D., 2008. Surface wave array tomography in SE Tibet from ambient seismic noise and two-station analysis—II. Crustal and upper-mantle structure, *Geophys. J. Int.*, **173**(1), 205–219.
- Yao, H., van der Hilst, R.D. & Montagner, J.-P., 2010. Heterogeneity and anisotropy of the lithosphere of SE Tibet from surface wave array tomography, *J. geophys. Res.*, **115**(B12), doi:10.1029/2009JB007142.
- Yin, A. & Harrison, T.M., 2000. Geologic evolution of the Himalayan-Tibetan Orogen, *Annu. Rev. Earth planet. Sci.*, **28**(1), 211–280.
- Yuan, D.-Y. *et al.*, 2013. The growth of northeastern Tibet and its relevance to large-scale continental geodynamics: a review of recent studies, *Tectonics*, **32**(5), 1358–1370.
- Yue, H. *et al.*, 2012. Lithospheric and upper mantle structure of the northeastern Tibetan Plateau, *J. geophys. Res.*, **117**, 1–18.
- Zhang, P.-Z. *et al.*, 2004. Continuous deformation of the Tibetan Plateau from global positioning system data, *Geology*, **32**(9), 809–812.
- Zhao, W. *et al.*, 2001. Crustal structure of central Tibet as derived from project INDEPTH wide-angle seismic data, *Geophys. J. Int.*, **145**(2), 486–498.